

Interference of dynamical arrest, thermodynamic instabilities and energy-scale competition in symmetric binary mixtures

R. Peredo-Ortiz,¹ E. Lázaro-Lázaro,¹ M. Medina-Noyola,¹ and L.F. Elizondo-Aguilera²

¹*Instituto de Física, Universidad Autónoma de San Luis Potosí,
Álvaro Obregón 64, 78000 San Luis Potosí, México*

²*Monte Caldera Technologies Inc., 12 N Cheyenne Ave, Tulsa, Oklahoma, USA*
(Dated: May 15, 2026)

The equilibrium behavior of binary mixtures can be understood through the competition of energy scales, which classifies their corresponding phase diagrams into distinct topological regimes (Types I–IV). However, in many soft-matter mixtures, strong competing interactions and kinetic barriers often promote dynamical arrest, disrupting the formation of equilibrium and metastable states, and thus rendering conventional phase diagrams incomplete. Here we extend the description and classification of binary systems inside regions of thermodynamical instability. Specifically, we discuss how the interplay between two kind of instabilities and kinetic arrest generates a variety of amorphous states driven by different underlying mechanisms. For strong cross-attraction, for example, dynamical arrest suppresses demixing, whereas in competitive regimes, a mixture may display either condensation-driven or demixing-induced arrested states. The crossover between these regimes can be described by a structural order parameter χ , providing a unified non-equilibrium description that reconciles theoretical predictions with experimentally observed arrested states.

The formation of amorphous, dynamically-arrested states in binary mixtures is governed by the interplay of competing physical scales. For example, in the paradigmatic case of size-asymmetric systems – such as colloid-polymer, or hard-sphere binary mixtures – the physical mechanisms underlying dynamical arrest emerge from competition in length scales. As the size-ratio $\delta = \sigma_A/\sigma_B$ decreases, the increasing disparity in geometric packing induces a bifurcation of the glass transition (GT), giving rise to the formation of different dynamically-arrested states such as repulsive (caging-driven) glasses, attractive (depletion-driven) glasses, and double glasses, in which the two species may arrest sequentially [1–5]. Thus, in these mixtures, size-asymmetry determines the nature of the resulting amorphous states, which is explicitly governed by steric frustration between its components [6–12].

In parallel, the description and classification of equilibrium phases in binary mixtures with attractive interactions stand as a foundational achievement of statistical thermodynamics. As first established by van Konynenburg and Scott [13–15] – and later formalized by Chen and Forstmann [16] – the topology of the phase diagram is dictated by the energy-scale competition between self-species attraction (ϵ_{ii}) and cross-species attraction (ϵ_{ij} , $i \neq j$). Depending on the energy-ratio $\alpha = \epsilon_{ij}/\epsilon_{ii}$, the landscape of thermodynamic instability is fully determined: high α favors gas-liquid (GL) condensation, while low α favors liquid-liquid (LL) demixing. From a purely thermodynamic point of view, this discussion is well established: the instability temperatures – the spinodal, describing GL condensation (T_s), and the λ -line, for LL demixing (T_λ) – strictly delimit the boundaries of the stable fluid phase [14–22].

However, in many soft matter mixtures – such as colloidal suspensions and protein solutions – the thermody-

amic phase diagram represents only an idealized limit of a more general non-equilibrium scenario. Experimental evidence [23–29], for example, demonstrates that when such mixtures are quenched into their metastable regimes, the thermodynamic driving forces responsible for phase separation and demixing are often hindered by dynamical arrest mechanisms. Consequently, standard equilibrium phase diagrams are insufficient to represent the experimental reality of these arrested mixtures, where the observed “final states” are the result of an intricate competition between instability and kinetic constraints [5, 30, 31].

To bridge this gap in the characterization of binary mixtures, thus, one requires a theoretical framework capable of extending their physical description into non-equilibrium domains, particularly below the aforementioned instability surfaces. To this end, here we employ the non-equilibrium self-consistent generalized Langevin equation (NESCGLE) theory [32–35] (summarized in Sec. **S1** of the Supplementary Material (SM)) to characterize the irreversible evolution of binary mixtures quenched into different metastable domains. Standard equilibrium theories of dynamic arrest treat thermodynamic instability surfaces merely as singularities that delimit *inaccessible* domains in the control-parameters space [36–38]. In contrast, NESCGLE extends this framework by also utilizing these surfaces as boundary conditions for arrested dynamics and non-equilibrium relaxation [30, 31, 39–41]

Specifically, we employ this framework to characterize symmetric binary mixtures (SBM, $\sigma_A = \sigma_B$) governed by attractive forces and with a different energy ratio α . This allows us to explore the resulting thermodynamic instability and dynamical arrest surfaces within the full concentration-density-temperature (c, ρ, T) space

(see Secs. **S2** and **S3** of the SM for details). Our central finding is that energy-scale competition generates a rich variety of non-equilibrium states in SBM, as a result of the interference between GL separation, LL demixing and dynamical arrest transitions, ultimately determined by the energy-scale ratio α . Hence, just as size asymmetry (δ) partitions the glassy-states diagrams into repulsive, mixed, and attractive glasses domains [2, 4, 5], here we show that energy competition (α) partitions the SBM diagrams into distinct kinetic regimes.

Employing NESCGLE we construct a “Kinetic Atlas” (detailed in Sec. **S3** of the SM) that depicts the interplay between two thermodynamic instabilities (GL and LL) and different kinetic arrest mechanisms. This elucidates how the complex interplay between the spinodal surface $T_s(\rho, c)$ (density instability), the λ -surface $T_\lambda(\rho, c)$ (concentration instability), and the dynamic arrest surface $T_c(\rho, c)$ is dictated by the energy scale ratio α . Importantly, our analysis of the asymptotic localization lengths reveals that the GT surface T_c does not end at the intersection with the spinodal surface – nor at the intersection with the surface $T_\lambda(\rho, c)$ – instead, it penetrates deep into the metastable regions, similar to the scenario found for monodisperse cases [39–41].

As detailed in Sec. **S4** of the SM (see Fig. S7), this extension of T_c manifests itself as a “gel-glass” transition line: a dynamic boundary separating the region of microscopically caged “attractive glasses” from the mesoscopically arrested “gels” formed via interrupted spinodal decomposition [39, 40, 42, 43]. In turn, this transition line defines the kinetic evolution and final state of a mixture after quenching below the instability surface. Since the complete three-dimensional topology of an SBM is somehow intricate, we shall restrict ourselves to consider – without loss of generality – equimolar concentrations ($c = 0.5$), to highlight the most distinctive outcomes introduced by energy competition. For concreteness, from now on we will consider an SBM described by hard-sphere plus square-well (HSSW) interactions (see Sec. **S2** of the SM for details).

First, let us discuss the case of relatively strong cross-attractions, $\alpha = 0.8$ (Fig. 1a), in which the strengths of self (ϵ_{ii}) and cross-interactions (ϵ_{ij}) are comparable, so that the mixture is expected to resemble features of a monodisperse ($\alpha = 1$) system [39, 40]. By analyzing the $k \rightarrow 0$ limit of the elements $M_{\rho\rho}(k)$, $M_{cc}(k)$, and $M_{c\rho}(k)$ of the stability matrix $\mathbf{M}(k)$ (see Subsection S2.1 of the SM), one can directly determine the instability boundaries $T_s(\rho)$ and $T_\lambda(\rho)$. These correspond to the spinodal and λ -lines, shown as red solid-dashed and green dashed lines in Fig. 1, respectively. Here, both curves intersect at the thermodynamic critical end point (CEP), $(\rho_{\text{CEP}}, T_{\text{CEP}})$ (solid diamond). This intersection defines two distinct density regimes: (i) for $\rho < \rho_{\text{CEP}}$, $T_s > T_\lambda$, meaning GL condensation precedes LL demixing upon cooling; and (ii) for $\rho > \rho_{\text{CEP}}$, $T_\lambda > T_s$, where

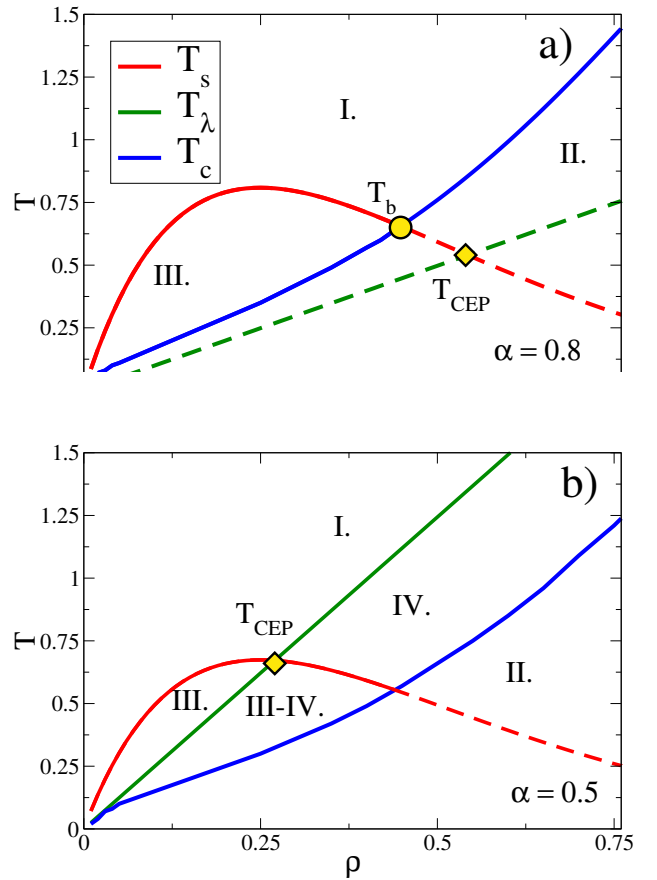


FIG. 1. The competition between thermodynamic instability and dynamical arrest. (a) **Kinetic Suppression** ($\alpha = 0.8$): Strong cross-attraction causes the arrest line T_c (blue) to detach from and remain strictly above the demixing instability (green). The system vitrifies into a homogeneous glass, kinetically masking the demixing region. (b) **Emergent Demixing** ($\alpha = 0.5$): Weaker cross-attraction allows the demixing line to pierce the arrest line, creating a window for gelation.

LL demixing obliterates GL condensation.

To determine the locus of the dynamical arrest transition lines for the HSSW-SBM with $\alpha = 0.8$, we evaluate the behavior of the NESCGLE ergodicity parameters, $\gamma_A^{(a)}$ and $\gamma_B^{(a)}$ (the interested reader is referred to Sec. **S4** of the SM for a detailed description of this methodology). This analysis reveals that the dynamic arrest temperature $T_c(\rho)$ intersects the spinodal line $T_s(\rho)$ at a bifurcation temperature point T_b , which remains strictly higher than the CEP where LL demixing and GL condensation would coexist [14]. For $\rho \leq \rho_b < \rho_{\text{CEP}}$, this arrest transition virtually coincides with $T_s(\rho)$ (superposed red solid line)—a behavior closely analogous to that of monodisperse systems [35, 39, 40]. Beyond this bifurcation, however, $T_c(\rho)$ completely envelopes the λ -line (T_λ), burying it deep within the non-ergodic region.

From a kinetic perspective, this topology has profound physical implications. Upon quenching, the system vit-

rifies into a homogeneous glass *before* it can access the LL demixing instability. This theoretical finding successfully rationalizes the experimental difficulty in observing demixing in strongly attractive colloidal mixtures: while the thermodynamic driving force is present, the slow kinetics effectively suppress its macroscopic expression [27, 29, 44].

Second, by reducing the energy ratio to $\alpha = 0.5$ (Fig. 1b), the demixing instability T_λ rises above the arrest line. In this case, the potential well is deeper for self-interactions (ϵ_{ii}) than for cross-interactions (ϵ_{ij}), promoting the segregation of like-species. Thermal fluctuations easily break the weaker bonds between unlike species, driving the system to agglomerate into compositionally distinct domains. Here, a competitive regime emerges where phase separation precedes arrest. This recovers the “arrested demixing” scenario described by Varrato et al. [27], leading to the formation of bicontinuous bigels rather than homogeneous glasses. This formation of compositionally distinct domains is consistent with the domain growth laws observed in simulations of quenched symmetric mixtures, where phase segregation precedes the eventual kinetic arrest [21, 22].

Based on the thermodynamic landscape and the kinetic fates, we classify the thermodynamic space (ρ, T) into four distinct regions: **I.** Homogeneous Mixed Fluid, **II.** Homogeneous Double Glass, **III.** Heterogeneous Mixed Structures (Condensation Gel), and **IV.** Demixed Homogeneous Fluid. In Region I, thermodynamic conditions ensure homogeneity and kinetics ensure ergodicity. Region II is the counterpart: after a quench, the system remains homogeneous and mixed but is trapped in a frozen configuration, kinetically suppressing any thermodynamic drive for GL condensation or LL demixing (dashed lines in Figure 1). In Region III, the spinodal line T_s lies above the critical line T_c ; thermodynamics dominates kinetics, allowing the system to condense into a heterogeneous arrested gel. Analogously, in Region IV, kinetic conditions permit demixing, where species form uniform domains. The boundary separating homogeneous glass (Region II) from gel-forming regions (III and IV) is defined by a sharp and discontinuous jump in the asymptotic localization length γ (More details in SM section **S4**). This discontinuous dynamic transition marks the abrupt expansion of the dynamical cage of the particle from the microscopic scale characteristic of the attractive glass to the mesoscopic confinement length of the gel [39]. Unlike a smooth crossover, this boundary represents a distinct change in the topology of the arrested state. Finally, a crossover region exists between III and IV where both instabilities are active: the system is in a condition to simultaneously condense and demix, requiring a more detailed structural analysis.

Classifying this crossover region is experimentally challenging due to “structural blindness”: standard partial structure factors $S_{ii}(k)$ often display qualitatively degenerate

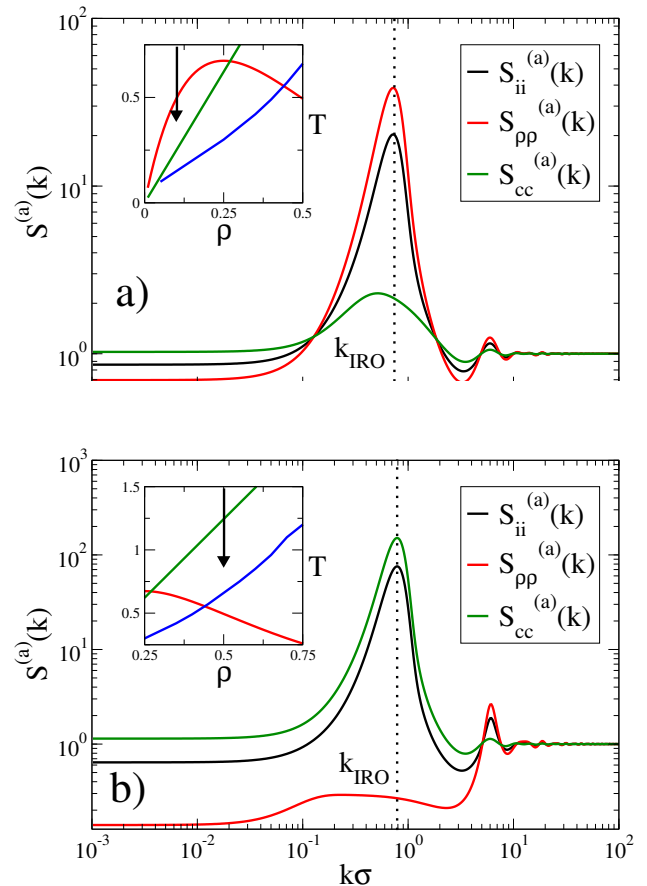


FIG. 2. Resolution of Structural Blindness via the Number-Concentration formalism ($\alpha = 0.5$). (a) In the condensation regime, the low- k peak is driven by density fluctuations $S_{\rho\rho}$ (red). (b) In the demixing regime, the peak is driven by concentration fluctuations S_{cc} (green). Note that the standard partial structure factors S_{ii} (black lines) appear qualitatively identical, illustrating structural blindness.

erate low-wave-vector peaks regardless of the underlying mechanism [21, 22]. Because the peak intensity depends on the specific quench depth, a low- k feature observed in $S_{ii}(k)$ is ambiguous—it could arise from either incipient gelation or phase separation. Standard partial structure factors are defined as

$$S_{ii}(k; t) = \frac{1}{N} \langle \delta\rho_i(\mathbf{k}, t) \delta\rho_i(-\mathbf{k}, t) \rangle. \quad (1)$$

These functions are “blind” to the distinction between condensation and demixing. For instance, while colloid-polymer mixtures are driven by a demixing instability [45, 46], the scattering signal from the dispersed colloids exhibits a low- k peak that is qualitatively indistinguishable from that observed during condensation-driven cluster formation [26, 47, 48].

To highlight this effect, we focus our discussion on the case $\alpha = 0.5$, where regions III and IV appear. As shown in Fig. 2, the asymptotic structure factors $S_{ii}^{(a)}(k) \equiv \lim_{t \rightarrow \infty} S_{ii}(k; t)$ —which diverge from

the equilibrium structure $S_{ii}^{(eq)}(k)$ to become protocol-dependent state functions inside the arrested region—exhibit a prominent peak at low wavevectors, $k_{IRO} \simeq 0.5$. This peak, indicative of mesoscopic Intermediate Range Order (IRO) structures [41, 47], is significantly higher than the main structural peak at $k_{main} \simeq 2\pi$ (i.e., $S_{ii}^{(a)}(k_{IRO}) > S_{ii}^{(a)}(k_{main})$). To resolve this ambiguity, we employ the number-concentration formalism [16, 49], where the transformation is defined by

$$S_{\rho\rho}^{(a)}(k) = c_A S_{AA}^{(a)}(k) + c_B S_{BB}^{(a)}(k) + 2\sqrt{c_A c_B} S_{AB}^{(a)}(k) \quad (2)$$

$$S_{cc}^{(a)}(k) = c_B S_{AA}^{(a)}(k) + c_A S_{BB}^{(a)}(k) - 2\sqrt{c_A c_B} S_{AB}^{(a)}(k) \quad (3)$$

where c_i are the molar fractions.

As shown in Fig. 2, this transformation reveals a dramatic *inversion of roles*. For a quench into the condensation-driven regime (Region III, Fig. 2a), the low- k structure is dominated by total density fluctuations ($S_{\rho\rho}^{(a)}$), while concentration fluctuations ($S_{cc}^{(a)}$) exhibit a signal at least one order of magnitude lower. In the demixing regime (Region IV, Fig. 2b), the structure provided by the quench is dominated by concentration fluctuations, and density fluctuations are restricted to explaining the main peak. We show that while partial structure factors $S_{ii}^{(a)}(k)$ degrade in intensity, the dominance of $S_{\rho\rho}^{(a)}(k)$ (in condensation) versus $S_{cc}^{(a)}(k)$ (in demixing) follows the signature of the arrested structure. The relation of the correlations determined by the IRO peak, obtained from the global maximum of $S_{ii}^{(a)}(k)$, is key to addressing the classification of the intermediate region III-IV.

To visualize the complete landscape of amorphous solidification for $\alpha = 0.5$, Fig. 3(a) presents the 3D thermodynamic instability surface, colored by the equilibrium instability angle $|\theta|$ (defined in [16] and the section **S3** of SM). This angle predicts the system's *tendency* at the onset of instability: darker regions ($|\theta| \rightarrow \pi/2$) indicate a drive toward condensation, while lighter regions ($|\theta| \rightarrow 0$) indicate a drive toward demixing. However, this thermodynamic prediction is valid only **on** the surface; it cannot describe the final state of a system quenched deep into the arrested region (below the blue wireframe T_c of Fig. 3a).

To resolve the state of the material deep within the arrested regime, we define the metric χ , evaluated at the low- k peak wavevector k_{IRO} :

$$\chi = \frac{S_{\rho\rho}^{(a)}(k_{IRO})}{S_{\rho\rho}^{(a)}(k_{IRO}) + S_{cc}^{(a)}(k_{IRO})}. \quad (4)$$

Figure 3(b) maps a slice of the Kinetic Atlas for the equimolar concentration and the cross-interaction parameter $\alpha = 0.5$ [same as Fig. 1(b)]. The smooth gradient from the darker region $\chi \rightarrow 1$ (condensation) to

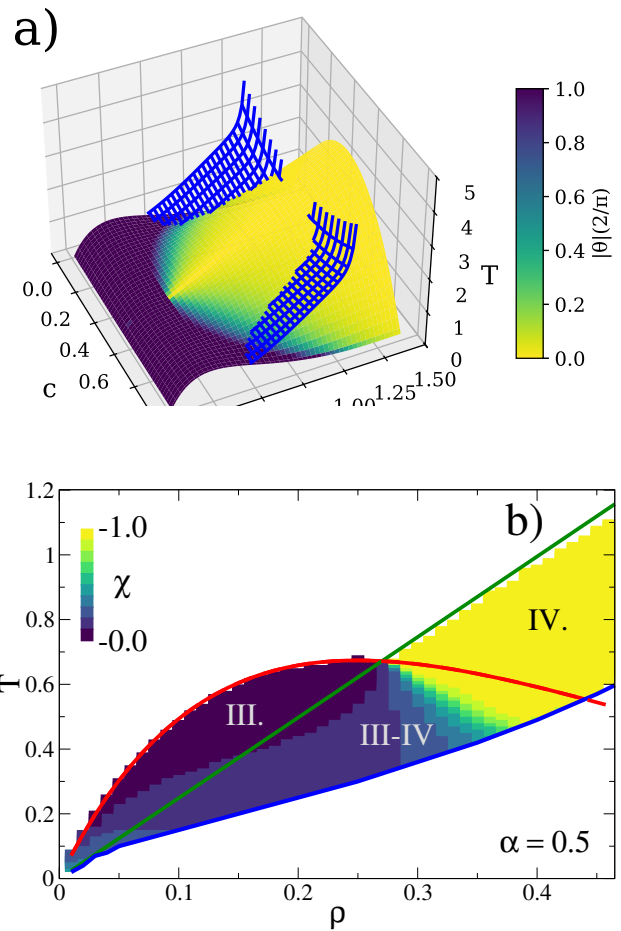


FIG. 3. From Thermodynamic Instability to Non-Equilibrium Arrest. (a) **Thermodynamic Prediction:** The 3D instability surface colored by the equilibrium instability angle $|\theta|$ (Dark = Condensation, Light = Demixing). The blue wireframe indicates the dynamic arrest surface T_c . Thermodynamics predicts the driving force only at the instability limit. (b) **Non-Equilibrium Reality:** A cross-section of the Kinetic Atlas at $c = 0.5$ for $\alpha = 0.5$, classified by the structural order parameter χ . Here, the energy scale α is tuned to allow demixing. The metric χ acts as the non-equilibrium extension of θ , classifying the state deep into the arrested region. The color gradient visualizes the continuous morphological transition from density-driven gels ($\chi \rightarrow 1$) to concentration-driven gels ($\chi \rightarrow 0$).

the lighter region $\chi \rightarrow 0$ (demixing) confirms that the non-equilibrium kinetic landscape is continuous. We observe that the transition region III-IV is invaded by its neighboring regions. The condensation region III and the demixing region IV enter into the transition region, marking the result of the competition of the instabilities. The frontier between III and IV is blurred by the continuous transition marked by χ . This metric provides a unified language to classify soft solids in binary mixtures, replacing geometric parameters (δ) with energetic ones (α).

We find that χ acts as the non-equilibrium extension of θ . On the instability line, χ recovers the thermodynamic prediction. Below the line, where thermodynamics is silent, χ continuously classifies the resulting soft solid. The map reveals a smooth crossover from condensation-driven gels (Region III, $\chi \approx 1$) to demixing-driven gels (Region IV, $\chi \approx 0$).

In summary, we have established that *energy scale competition* in symmetrical mixtures is the physical counterpart to *length scale competition* in asymmetric systems. However, this analogy reveals a distinct kinetic consequence: just as geometric frustration fractures the glass diagram in the latter, energetic frustration drives the phenomenon of *Kinetic Suppression* in the former. The χ metric introduced here provides a unified non-equilibrium phase map that reconciles the rigorous thermodynamic classification of binary mixtures with the complex kinetic reality of soft matter arrest. Our χ metric's ability to identify the nature of the arrested phase complements the structural and scaling analyses proposed for phase transitions in symmetric systems, extending their applicability into the deep non-equilibrium regime [21, 22].

The theoretical scenario presented here opens clear pathways for future research. While this work focused on structural properties, the mechanical characterization of these states is equally critical. Future work will extend the NESCGLE framework to calculate time-dependent viscoelastic properties, such as storage $G'(\omega; t)$ and loss $G''(\omega; t)$ moduli [50], allowing us to directly correlate the microstructural fingerprints identified here (the χ metric) with specific rheological signatures.

Finally, while our results assume instantaneous quenches, the *Kinetic Suppression* mechanism (Fig. 1a) suggests that slow cooling is necessary to bypass the glass ceiling and access the demixing region in Type I systems. We hypothesize that introducing a finite cooling rate $r_c = -dT/dt$ could fundamentally alter the kinetic competition described in our Kinetic Atlas [28, 51, 52]. In regimes of kinetic suppression, a sufficiently slow cooling rate might allow concentration fluctuations to ripen significantly before the arrest line is crossed, potentially stabilizing exotic non-equilibrium phases such as a “demixed double glass” or a bicontinuous bigel [53, 54]. Unlocking these protocol-dependent pathways represents the next frontier in the non-equilibrium physics of soft matter.

This work was supported by the Secretaría de Ciencia, Humanidades, Tecnología e Innovación (SE-CIHTI) through Postdoctoral Fellowships Grants No. I1200/224/2021 and I1200/320/2022. This work was also supported by the Laboratorio Nacional de Ingeniería de la Materia Fuera de Equilibrio (LANIMFE).

-
- [1] Yaakov Rosenfeld. Free-energy model for the inhomogeneous hard-sphere fluid mixture and density-functional theory of freezing. *Phys. Rev. Lett.*, 63:980–983, Aug 1989.
 - [2] R. Juárez-Maldonado and M. Medina-Noyola. Alternative view of dynamic arrest in colloid-polymer mixtures. *Phys. Rev. Lett.*, 101:267801, Dec 2008.
 - [3] Roland Roth. Fundamental measure theory for hard-sphere mixtures: a review. *Journal of Physics: Condensed Matter*, 22(6):063102, Jan 2010.
 - [4] Th. Voigtmann. Multiple glasses in asymmetric binary hard spheres. *Europhysics Letters*, 96(3):36006, Oct 2011.
 - [5] E. Lázaro-Lázaro, J. A. Moreno-Razo, and M. Medina-Noyola. Anomalous dynamic arrest of non-interacting spheres (“polymer”) diluted in a hard-sphere (“colloid”) liquid. *The Journal of Chemical Physics*, 148(10):104505, 03 2018.
 - [6] P. Bartlett and P.N. Pusey. Freezing of binary mixtures of hard-sphere colloids. *Physica A: Statistical Mechanics and its Applications*, 194(1):415–423, 1993.
 - [7] W. C. K. Poon and P. B. Warren. Phase behaviour of hard-sphere mixtures. *Europhysics Letters*, 28(7):513, Dec 1994.
 - [8] W. C. K. Poon and P. N. Pusey. *Phase Transition of Spherical Colloids*, pages 3–51. Springer Netherlands, Dordrecht, 1995.
 - [9] Marjolein Dijkstra, René van Roij, and Robert Evans. Phase diagram of highly asymmetric binary hard-sphere mixtures. *Phys. Rev. E*, 59:5744–5771, May 1999.
 - [10] T. Eckert and E. Bartsch. Re-entrant glass transition in a colloid-polymer mixture with depletion attractions. *Phys. Rev. Lett.*, 89:125701, Aug 2002.
 - [11] S. Ramakrishnan, M. Fuchs, K. S. Schweizer, and C. F. Zukoski. Entropy driven phase transitions in colloid-polymer suspensions: Tests of depletion theories. *The Journal of Chemical Physics*, 116(5):2201–2212, 02 2002.
 - [12] Anna Kozina, Dominik Sagawe, Pedro Díaz-Leyva, Eckhard Bartsch, and Thomas Palberg. Polymer-enforced crystallization of a eutectic binary hard sphere mixture. *Soft Matter*, 8:627–630, 2012.
 - [13] P. H. van Konynenburg and R. L. Scott. Critical lines and phase equilibria in binary van der Waals mixtures. *Philosophical Transactions of the Royal Society of London, Series A: Mathematical and Physical Sciences*, 298(1442):495–540, 12 1980.
 - [14] Jürgen Köfinger, Nigel B. Wilding, and Gerhard Kahl. Phase behavior of a symmetrical binary fluid mixture. *The Journal of Chemical Physics*, 125(23):234503, 12 2006.
 - [15] Elisabeth Schöll-Paschinger and Gerhard Kahl. Type-iv phase behavior in fluids with an internal degree of freedom. *The Journal of Chemical Physics*, 123(13):134508, 10 2005.
 - [16] X. S. Chen and F. Forstmann. The demixing and gas-liquid instability of a binary Yukawa fluid. *The Journal of Chemical Physics*, 97(5):3696–3703, 09 1992.
 - [17] G. Pellicane, F. Saija, C. Caccamo, and P. V. Giaquinta. Thermodynamic stability of fluid-fluid phase separation in binary athermal mixtures: the role of nonadditivity. *The Journal of Physical Chemistry B*, 110(9):4359–4364,

- Mar 2006.
- [18] J. P. Hansen and I. R. McDonald. *Theory of Simple Liquids*. Academic Press Inc., 1976.
- [19] J. Köfinger, G. Kahl, and N. B. Wilding. Phase behaviour of a symmetrical binary mixture in a field. *Europhysics Letters*, 75(2):234, jun 2006.
- [20] Enrique Diaz-Herrera, Guillermo Ramirez-Santiago, and Jose A. Moreno-Razo. Phase and interfacial behavior of partially miscible symmetric lennard-jones binary mixtures. *The Journal of Chemical Physics*, 123(18):184507, 11 2005.
- [21] Subir K. Das, Jürgen Horbach, and Kurt Binder. Transport phenomena and microscopic structure in partially miscible binary fluids: A simulation study of the symmetrical lennard-jones mixture. *The Journal of Chemical Physics*, 119(3):1547–1558, 07 2003.
- [22] Subir K. Das, Jürgen Horbach, Kurt Binder, Michael E. Fisher, and Jan V. Sengers. Static and dynamic critical behavior of a symmetrical binary fluid: A computer simulation. *The Journal of Chemical Physics*, 125(2):024506, 07 2006.
- [23] Hartmut Löwen. Possibilities of phase separation in colloidal suspensions. *Physica A: Statistical Mechanics and its Applications*, 235(1):129–141, 1997. Proceedings of the Workshop on Colloid Physics.
- [24] Francesco Sciortino, Sergey V. Buldyrev, Cristiano De Michele, Giuseppe Foffi, Neda Ghofraniha, Emilia La Nave, Angel Moreno, Stefano Mossa, Ivan Saika-Voivod, Piero Tartaglia, and Emanuela Zaccarelli. Routes to colloidal gel formation. *Computer Physics Communications*, 169(1):166–171, 2005. Proceedings of the Europhysics Conference on Computational Physics 2004.
- [25] Emanuela Zaccarelli. Colloidal gels: equilibrium and non-equilibrium routes. *Journal of Physics: Condensed Matter*, 19(32):323101, jul 2007.
- [26] Hongyu Guo, S. Ramakrishnan, James L. Harden, and Robert L. Leheny. Gel formation and aging in weakly attractive nanocolloid suspensions at intermediate concentrations. *The Journal of Chemical Physics*, 135(15):154903, 10 2011.
- [27] Francesco Varrato, Lorenzo Di Michele, Maxim Belushkin, Nicolas Dorsaz, Simon H. Nathan, Erika Eiser, and Giuseppe Foffi. Arrested demixing opens route to bigels. *Proceedings of the National Academy of Sciences*, 109(47):19155–19160, 2012.
- [28] Lilian C. Hsiao and Patrick S. Doyle. Celebrating soft matter’s 10th anniversary: Sequential phase transitions in thermoresponsive nanoemulsions. *Soft Matter*, 11:8426–8431, 2015.
- [29] James L. Harden, Hongyu Guo, Martine Bertrand, Tyler N. Shendruk, Subramanian Ramakrishnan, and Robert L. Leheny. Enhanced gel formation in binary mixtures of nanocolloids with short-range attraction. *The Journal of Chemical Physics*, 148(4):044902, 01 2018.
- [30] Nohely Benitez-Camacho, José Manuel Olais-Govea, Leticia López-Flores, and Honorina Ruiz-Estrada. Arrested spinodal decomposition of the screened symmetric restricted primitive model. *The Journal of Chemical Physics*, 159(4):044906, 07 2023.
- [31] Juan C. Avilés-Sánchez, Ernesto C. Cortés-Morales, Mariana E. Farías-Anguiano, Jonathan K. Whitmer, and Pedro E. Ramírez-González. Linking dynamics and structure in highly asymmetric ionic liquids. *Physics of Fluids*, 37(1):017173, 01 2025.
- [32] M Medina-Noyola and Pedro Ramírez-González. Nonequilibrium relaxation and near-arrest dynamics in colloidal suspensions. *Journal of Physics: Condensed Matter*, 21(50):504103, nov 2009.
- [33] Pedro Ramírez-González and Magdaleno Medina-Noyola. General nonequilibrium theory of colloid dynamics. *Phys. Rev. E*, 82:061503, Dec 2010.
- [34] Ricardo Peredo-Ortiz, Luis F. Elizondo-Aguilera, Pedro Ramírez-González, Edilio Lázaro-Lázaro, Patricia Mendoza-Méndez, and Magdaleno Medina-Noyola. Nonequilibrium onsager–machlup theory. *Molecular Physics*, 0(0):e2297991, 2023.
- [35] R. Peredo-Ortiz, E. Lázaro-Lázaro, O. Joaquín-Jaime, M. Medina-Noyola, and L.F. Elizondo-Aguilera. The nonequilibrium self-consistent generalized langevin equation theory of glasses and gels. *Annual Review of Chemical and Biomolecular Engineering*, 2026.
- [36] R. Evans. The nature of the liquid-vapour interface and other topics in the statistical mechanics of non-uniform, classical fluids. *Advances in Physics*, 28(2):143–200, 1979.
- [37] Wolfgang Götze. *Complex Dynamics of Glass-Forming Liquids: A Mode-Coupling Theory*. Oxford University Press, London, England, May 2009.
- [38] Laura Yeomans-Reyna and Magdaleno Medina-Noyola. Self-consistent generalized langevin equation for colloid dynamics. *Phys. Rev. E*, 64:066114, Nov 2001.
- [39] José Manuel Olais-Govea, Leticia López-Flores, and Magdaleno Medina-Noyola. Non-equilibrium theory of arrested spinodal decomposition. *The Journal of Chemical Physics*, 143(17):174505, 11 2015.
- [40] Jesús Benigno Zepeda-López and Magdaleno Medina-Noyola. Waiting-time dependent non-equilibrium phase diagram of simple glass- and gel-forming liquids. *The Journal of Chemical Physics*, 154(17):174901, 05 2021.
- [41] Ana Gabriela Carretas-Talamante, Jesús Benigno Zepeda-López, Edilio Lázaro-Lázaro, Luis Fernando Elizondo-Aguilera, and Magdaleno Medina-Noyola. Non-equilibrium view of the amorphous solidification of liquids with competing interactions. *The Journal of Chemical Physics*, 158(6):064506, 02 2023.
- [42] José Manuel Olais-Govea, Leticia López-Flores, Martín Chávez-Páez, and Magdaleno Medina-Noyola. Nonequilibrium kinetics of the transformation of liquids into physical gels. *Phys. Rev. E*, 98:040601, Oct 2018.
- [43] José Manuel Olais-Govea, Leticia López-Flores, Jesús Benigno Zepeda-López, and Magdaleno Medina-Noyola. Interference between the glass, gel, and gas-liquid transitions. *Scientific Reports*, 9(1):16445, Nov 2019.
- [44] Isla Zhang, C. Patrick Royall, Malcolm A. Faers, and Paul Bartlett. Phase separation dynamics in colloid–polymer mixtures: the effect of interaction range. *Soft Matter*, 9:2076–2084, 2013.
- [45] Matthias Schmidt, Hartmut Löwen, Joseph M Brader, and Robert Evans. Density functional theory for a model colloid–polymer mixture: bulk fluid phases. *Journal of Physics: Condensed Matter*, 14(40):9353, sep 2002.
- [46] S. A. Shah, S. Ramakrishnan, Y. L. Chen, K. S. Schweizer, and C. F. Zukoski. Scattering studies of the structure of colloid-polymer suspensions and gels. *Langmuir*, 19(12):5128–5136, Jun 2003.
- [47] Jianlan Wu, Yun Liu, Wei-Ren Chen, Jianshu Cao, and Sow-Hsin Chen. Structural arrest transitions in flu-

- ids described by two yukawa potentials. *Phys. Rev. E*, 70:050401, Nov 2004.
- [48] N. Dorsaz, G. M. Thurston, A. Stradner, P. Schurtenberger, and G. Foffi. Colloidal characterization and thermodynamic stability of binary eye lens protein mixtures. *The Journal of Physical Chemistry B*, 113(6):1693–1709, Feb 2009.
- [49] A. B. Bhatia and D. E. Thornton. Structural aspects of the electrical resistivity of binary alloys. *Phys. Rev. B*, 2:3004–3012, Oct 1970.
- [50] R. Peredo-Ortiz, O. Joaquín-Jaime, L. López-Flores, M. Medina-Noyola, and L. F. Elizondo-Aguilera. Nonequilibrium theory of the linear viscoelasticity of glass and gel forming liquids. *Journal of Rheology*, 69(2):201–222, 03 2025.
- [51] C. Patrick Royall and Alex Malins. The role of quench rate in colloidal gels. *Faraday Discuss.*, 158:301–311, 2012.
- [52] Scott M. Fenton, Poornima Padmanabhan, Brian K. Ryu, Tuan T. D. Nguyen, Roseanna N. Zia, and Matthew E. Helgeson. Minimal conditions for solidification and thermal processing of colloidal gels. *Proceedings of the National Academy of Sciences*, 120(25):e2215922120, 2023.
- [53] Ahmad Shakeel, Ujala Farooq, Tanveer Iqbal, Saima Yasin, Francesca R. Lupi, and Domenico Gabriele. Key characteristics and modelling of bigels systems: A review. *Materials Science and Engineering: C*, 97:932–953, 2019.
- [54] Araceli Martín-Illana, Fernando Notario-Pérez, Raúl Cazorla-Luna, Roberto Ruiz-Caro, Maria C. Bonferoni, Aitana Tamayo, and María D. Veiga. Bigels as drug delivery systems: From their components to their applications. *Drug Discovery Today*, 27(4):1008–1026, 2022.

Supplemental Material for:

Interference of dynamical arrest, thermodynamic instabilities
and energy-scale competition in symmetric binary mixtures

R. Peredo-Ortiz¹, E. Lázaro-Lázaro¹, M. Medina-Noyola¹, and L.F. Elizondo-Aguilera²

¹*Instituto de Física, Universidad Autónoma de San Luis Potosí,
Álvaro Obregón 64, 78000 San Luis Potosí, México*

²*Monte Caldera Technologies, 12 N Cheyenne Ave, Tulsa, Oklahoma, USA.*

May 15, 2026

S1 The NESCGLE theory

This supplemental material summarizes the fundamental concepts underlying the Non-Equilibrium Self-Consistent Generalized Langevin Equation (NESCGLE) theory [1, 2, 3]. We restrict our description to the governing equations for the waiting-time dependent structure factor, defined as $S_{ij}(k; t) \equiv (1/N) \langle \delta\rho_i(k, t) \delta\rho_j(-k, t) \rangle^{(ss)}$. The notation $\langle \dots \rangle^{ss}$ denotes an average over a stationary state, generalizing the standard thermodynamic equilibrium ensemble average [4]. Under thermodynamic equilibrium conditions, this structure factor is intimately related to the Stability Matrix, \mathcal{E}_{ij} , defined as:

$$\mathcal{E}_{ij}(k; \rho_A, \rho_B, T) \equiv \delta_{ij} - \sqrt{\rho_i \rho_j} c_{ij}(k), \quad (\text{S1.1})$$

where $c_{ij}(k)$ is the direct correlation function obtained from the Ornstein-Zernike Equation (OZE), once a closure relation is specified [5, 6]; and the diagonal density matrix $\sqrt{\rho}$ has elements defined as $\sqrt{\rho}_{ij} \equiv \delta_{ij} \sqrt{\rho_i}$.

In its simplest form, the NESCGLE theory provides a framework to compute the structural relaxation of a colloidal system following a sudden change in its thermodynamic state. The time evolution of the non-equilibrium structure factor, $\mathbf{S}(k; t)$ is governed by the dynamic law:

$$\begin{aligned} \frac{\partial \mathbf{S}(k; t)}{\partial t} = & \mathbf{H}(t) \cdot \left\{ \mathbf{S}(k; t) - \left[\sqrt{\rho^{(f)}} \cdot \boldsymbol{\varepsilon} \cdot \sqrt{\rho^{(f)}} \right]^{-1} \right\} \\ & + \left\{ \mathbf{S}(k; t) - \left[\sqrt{\rho^{(f)}} \cdot \boldsymbol{\varepsilon} \cdot \sqrt{\rho^{(f)}} \right]^{-1} \right\} \cdot \mathbf{H}^\dagger(t), \end{aligned} \quad (\text{S1.2})$$

here the 2×2 relaxation rate matrix is defined as $\mathbf{H}(t) = -k^2 \mathbf{D}^0 \cdot \mathbf{b}(t) \cdot \left[\sqrt{\rho^{(f)}} \cdot \boldsymbol{\varepsilon} \cdot \sqrt{\rho^{(f)}} \right]$. The diagonal matrices \mathbf{D}^0 and $\mathbf{b}(t)$ represents the short-time self-diffusion coefficients and the time-dependent mobility functions of the particles, respectively.

The elements of the matrix $[\mathbf{b}(t)]_{ij} = \delta_{ij} b_{ii}(t)$ serve as the state parameters governing the dynamical system defined by Eq. (S1.2). The elements of the diagonal time-dependent mobility functions are evaluated as:

$$b_{ii}(t) = \left[1 + \int_0^\infty d\tau \Delta \zeta_{ii}(\tau; t) \right]^{-1}. \quad (\text{S1.3})$$

The friction memory functions, $\Delta\zeta_{ii}$ are obtained by solving the *Self-Consistent Scheme* (SCS), defined by the following system of equations:

$$\Delta\zeta_{ii}(\tau; t) = \frac{D_i^0}{3(2\pi)^3} \int d^3k k^2 \left[\mathbf{F}^{(s)}(k, \tau; t) \right]_{ii} \left[\mathbf{h}(k; t) \cdot \sqrt{\rho} \cdot \mathbf{S}^{-1}(k; t) \right. \\ \left. \cdot \mathbf{F}(k, \tau; t) \cdot \mathbf{S}^{-1}(k; t) \cdot \sqrt{\rho} \cdot \mathbf{h}(k; t) \right]_{ii}, \quad (\text{S1.4})$$

where the time-dependent total correlation matrix is given by $\mathbf{h}(k; t) = \sqrt{\rho^{-1}} \cdot (\mathbf{S}(k; t) - \mathbf{I}) \cdot \sqrt{\rho^{-1}}$. In Laplace space, the self- and collective intermediate scattering functions, $\mathbf{F}^{(s)}(k, \tau; t)$ and $\mathbf{F}(k, \tau; t)$, are given respectively by

$$\mathbf{F}^{(s)}(k, z; t) = \left\{ z\mathbf{I} + k^2 \mathbf{D}^0 \cdot [z\mathbf{I} + \mathbf{\Lambda}(k) \cdot \mathbf{\Delta}\zeta(z)]^{-1} \right\}^{-1}, \quad (\text{S1.5})$$

and

$$\mathbf{F}(k, z; t) = \left\{ z\mathbf{I} + k^2 \mathbf{D}^0 \cdot [z\mathbf{I} + \mathbf{\Lambda}(k) \cdot \mathbf{\Delta}\zeta(z; t)]^{-1} \cdot \mathbf{S}^{-1}(k; t) \right\}^{-1} \cdot \mathbf{S}^{-1}(k; t). \quad (\text{S1.6})$$

Here, the elements of the matrix $\mathbf{\Lambda}(k)$ are defined as $\Lambda_{ij}(k) = \delta_{ij}[1 + (k/k_i^{(c)})]$, where the empirical cut-off wave-vector is $k_i^{(c)} = 1.305(2\pi)/\sigma_i$. Within the NESCGLE, this parameter is employed to *calibrate* the theory for each specific application[7].

The Symmetric Binary Mixtures (SBM) offers the advantage of identical particle sizes, implying that the short-time self-diffusion coefficients are identical, $D_1^0 = D_2^0 = D^0$. Furthermore, at the equimolar concentration, $c = 0.5$, symmetry dictates that there is no physical distinction between the dynamics of the two species, leading to identical mobility functions, $b(t) = b_1(t) = b_2(t)$. However, dynamic asymmetry (one species arresting before the other) is excluded by symmetry in this specific study, but is a feature of the general theory. Consequently, the problem can be assigned to the same methodologies as previously defined for monodisperse systems [8].

Under these conditions, for an instantaneous quench from an initial temperature T_i ($t < 0$) to a final temperature T ($t > 0$), Eq. (S1.2) admits an analytic solution of the form

$$\mathbf{S}(k; u) = \left[\sqrt{\rho_f} \cdot \mathbf{\mathcal{E}}^{(f)} \cdot \sqrt{\rho_f} \right]^{-1} + \exp[-\mathbf{A}(k, u)] \\ \cdot \left\{ \mathbf{S}(k; t=0) - \left[\sqrt{\rho_f} \cdot \mathbf{\mathcal{E}}^{(f)} \cdot \sqrt{\rho_f} \right]^{-1} \right\} \cdot \exp[-\mathbf{A}^\dagger(k, u)]. \quad (\text{S1.7})$$

The decay matrix is defined as $\mathbf{A}(k, u) = uk^2 \mathbf{D}^0 \cdot [\sqrt{\rho_f} \cdot \mathbf{\mathcal{E}}^{(f)}(k) \cdot \sqrt{\rho_f}]$, where the stability matrix is a function of the final thermodynamic state $\mathbf{\mathcal{E}}^{(f)} = \mathbf{\mathcal{E}}(\rho_f, T_f)$. The material time, or *internal time*, $u(t)$ represents the accumulated mobility of the system and is defined as

$$u(t) = \int_0^t dt' b(t'). \quad (\text{S1.8})$$

Due to the symmetry at $c = 0.5$, the material times for both species are identical, $u(t) = u_1(t) = u_2(t)$, reflecting the symmetry of their respective mobilities, $b_{ii}(t) = b(t)$ [9].

A practical approach to studying the non-equilibrium properties of a system is to evaluate the asymptotic structure factor, defined as $\mathbf{S}^{(a)}(k) \equiv \mathbf{S}(k; t \rightarrow \infty)$. Under equilibrium conditions—specifically for temperatures situated above the condensation, demixing, and ideal glass transition lines—the system remains ergodic. Consequently, the material time diverges at long times $\lim_{t \rightarrow \infty} u(t) = \infty$. As a result, the elements of the decay matrix $\mathbf{A}(k, u)$ diverge, causing the exponential relaxation terms in Eq. (S1.7) to vanish. Thus, the asymptotic structure factor recovers the standard equilibrium form $\mathbf{S}^{(a)}(k) = [\sqrt{\rho_f} \cdot \mathbf{\mathcal{E}}^{(f)}(k) \cdot \sqrt{\rho_f}]^{-1} = \mathbf{S}^{eq}(k)$.

However, crossing any of the transition lines causes the asymptotic structure factor, $\mathbf{S}^{(a)}(k)$, to deviate from the equilibrium form $[\sqrt{\rho_f} \cdot \mathcal{E}^{(f)}(k) \cdot \sqrt{\rho_f}]^{-1}$. In this regime, $\mathbf{S}^{(a)}(k)$ becomes dependent on the specific preparation protocol used to reach the final thermodynamic state (ρ_f, T_f) [1, 2, 3]. To determine the asymptotic structure $\mathbf{S}^{(a)}(k)$, we must evaluate the localization lengths γ_i for species $i = A, B$, defined as the long-time asymptotic limits of the mean squared displacements, $\gamma_i \equiv \lim_{\tau \rightarrow \infty} \langle |\Delta \mathbf{r}_i(\tau)|^2 \rangle$.

These lengths are obtained by solving the following system of coupled bifurcation equations [10]:

$$\frac{1}{\gamma_i} = \frac{1}{3(2\pi)^3} \int d^3k k^2 [\mathbf{\Lambda}(\mathbf{\Lambda} + k^2\gamma)^{-1}]_{ii} \times \left[\mathbf{c}(t) \sqrt{\rho} \mathbf{S}(t) \mathbf{\Lambda}(\mathbf{S}(t) \mathbf{\Lambda} + k^2\gamma^{(a)})^{-1} \sqrt{\rho} \mathbf{h}(t) \right]_{ii}, \quad (\text{S1.9})$$

which are obtained in the asymptotic limit $\tau \rightarrow \infty$ of the SCS described by equations (S1.4)-(S1.6).

In our calculation, we replace the static structure factor in Eq. (S1.9) with the material-time dependent structure factor $\mathbf{S}(k; u)$ defined in Eq. (S1.7). Consequently, the localization length becomes a function of the material time, $\gamma = \gamma(u)$. Under equilibrium conditions, $\gamma(u)$ diverges for all u . However, under non-equilibrium conditions, there exists a finite value of u where the localization length transitions to a finite value[9]. This limiting value defines the asymptotic material time, $u^{(a)} \equiv \lim_{t \rightarrow \infty} u(t)$. As a result, the asymptotic localization length is given by $\gamma^{(a)} = \gamma(u^{(a)})$.

The solutions to Eq. (S1.9) reveal two distinct dynamical regimes: an *ergodic region* where $1/\gamma_i^{(a)} = 0$ (infinite localization length, fluid state), and a *non-ergodic region* where $1/\gamma_i^{(a)} > 0$ (finite localization length, arrested state). The boundary between these regions defines the *critical arrest temperature*, $T_c(\rho, c)$.

S2 Model System: The Symmetric Binary Mixture

This supplemental material provides methodological details related to the model of Symmetric Binary Mixture (SBM). We consider a binary mixture composed of N_A particles of species A and N_B particles of species B contained in a volume V . The total number density is given by $\rho = (N_A + N_B)/V$, and the molar fractions are defined as $x_i = N_i/(N_A + N_B)$ for $i = A, B$. For the SBM, the effective diameters of both species are equal, $\sigma_A = \sigma_B = \sigma$.

The thermodynamic behavior of this kind of mixture is determined by the pairwise interaction potential $U_{ij}(r)$. In this work, we specifically model the SBM using a Hard-Sphere plus Square-Well (HS-SW) potential, in which the interaction between species i and j is defined as:

$$U_{ij}(r) = \begin{cases} \infty & r < \sigma_{ij} \\ -\epsilon_{ij} & \sigma_{ij} \leq r < \lambda\sigma_{ij} \\ 0 & r \geq \lambda\sigma_{ij}, \end{cases} \quad (\text{S2.1})$$

where $\sigma_{AA} = \sigma_{BB} = \sigma_{AB} = \sigma_{BA} = \sigma$. The energy scales are defined such that $\epsilon_{AA} = \epsilon_{BB} = \epsilon$ (self-attraction) and $\epsilon_{AB} = \alpha\epsilon$ (cross-attraction). Hence, The parameter α determines the competition between condensation and demixing.

The thermodynamic behavior of this mixture is determined entirely by the pairwise interaction potentials, $U_{ij}(r)$. For the SBM model, this potential is decomposed into a repulsive hard-sphere (HS) core and an attractive tail, $\psi_{ij}(r)$:

$$U_{ij}(r) = U^{\text{HS}}(r) + \psi_{ij}(r). \quad (\text{S2.2})$$

Here, $U^{\text{HS}}(r)$ represents the standard hard-sphere potential for particles of diameter σ . The symmetry of the model dictates that the attractive interactions between *like species* are identical,

$\psi_{AA}(r) = \psi_{BB}(r) \equiv \psi(r)$, while the *cross-species interaction* is scaled by a parameter α , such that $\psi_{AB}(r) = \alpha\psi(r)$. Consequently, the thermodynamic stability and phase behavior of the system are controlled by the single parameter α , which quantifies the relative intensity of the cross-species attraction.

Two distinct regimes emerge based on the value of α . In the first case, $\alpha > 1$, the cross-interaction is stronger than the self-interactions, and the system exhibits only Gas-Liquid (GL) condensation [11]. The second case, $\alpha < 1$, presents a much richer phenomenology characterized by the competition between GL condensation and Liquid-Liquid (LL) demixing as a function of the thermodynamic state variables $c = x_A$ and ρ [11, 12, 13, 14, 15].

In this work, we model the SBM by the Hard-Sphere plus square-well (SW) potential:

$$U_{ij}(r) = \begin{cases} \infty & \text{for } r < \sigma_{ij}, \\ -\epsilon_{ij} & \text{for } \sigma_{ij} \leq r < \lambda_{ij}^{(SW)}, \\ 0 & \text{for } r \geq \lambda_{ij}^{(SW)}. \end{cases} \quad (\text{S2.3})$$

Here, ϵ_{ij} represents the energy scale of the interaction, with $\epsilon_{AA} = \epsilon_{BB} = \epsilon$ and $\epsilon_{AB} = \alpha\epsilon$. The parameter $\lambda_{ij}^{(SW)}$ defines the range of the attractive well. For this study, we fix this interaction range to $\lambda_{ij}^{(SW)} = 1.5\sigma$ for all pairs, in order to recover the previously studied case in the monodisperse limit[16].

S2.1 Thermodynamic Stability

We generalize the approach of Sharma and Sharma [17] to the case of binary mixtures. In their original work, the authors approximated the direct correlation function of a monodisperse colloidal system interacting via a hard-sphere plus square-well potential as the sum of a reference hard-sphere term and a perturbative attractive tail: $c(r) \approx c^{HS}(r) - \beta u^{SW}(r)$ [17]. Here, $c^{HS}(r)$ is the hard-sphere direct correlation function [18] and $u_{ij}^{SW}(r)$ is the attractive square-well potential. In thermodynamic equilibrium, the structure factor is determined entirely by this matrix via the relation (S1.1).

To determine the boundaries of thermodynamic stability (where the equilibrium relation $\mathbf{S}(k) = [\sqrt{\rho} \cdot \mathcal{E}(k) \cdot \sqrt{\rho}]^{-1}$ diverges), we analyze the eigenvalues of the stability matrix. Following Chen and Forstmann [11], the eigenvalues $\lambda_{1,2}(k)$ are given by:

$$\lambda_{1,2}(k) = \frac{\mathcal{E}_{AA}(k) + \mathcal{E}_{BB}(k) \mp \sqrt{[\mathcal{E}_{AA}(k) - \mathcal{E}_{BB}(k)]^2 + 4\mathcal{E}_{AB}^2(k)}}{2}. \quad (\text{S2.4})$$

The instability surface, marking the limit of stability, is defined by the condition where the smaller eigenvalue vanishes in the long-wavelength limit: $\lambda_1(k \rightarrow 0) = 0$.

A key advantage of the formalism developed by Chen and Forstmann [11] is the ability to transform these correlation functions from the particle-species basis into the collective basis of total number density ($\rho = \rho_1 + \rho_2$) and concentration ($c = \rho_1/\rho$) fluctuations. The transformed matrix $\mathbf{M}(k)$ has elements defined as:

$$M_{\rho\rho}(k) = c_1\mathcal{E}_{11}(k) + c_2\mathcal{E}_{22}(k) + 2\sqrt{c_1c_2}\mathcal{E}_{12}(k), \quad (\text{S2.5})$$

$$M_{cc}(k) = c_1c_2 [c_2\mathcal{E}_{11}(k) + c_1\mathcal{E}_{22}(k) - 2\sqrt{c_1c_2}\mathcal{E}_{12}(k)], \quad (\text{S2.6})$$

$$M_{\rho c}(k) = c_1c_2 [\mathcal{E}_{11}(k) - \mathcal{E}_{22}(k)] + \sqrt{c_1c_2}(c_2 - c_1)\mathcal{E}_{12}(k). \quad (\text{S2.7})$$

In the thermodynamic limit ($k \rightarrow 0$), these elements are directly related to the second derivatives of the Helmholtz and Gibbs free energy. Specifically, $M_{\rho\rho}$ relates to the Helmholtz free energy A via the isothermal compressibility:

$$\left. \frac{\partial^2(A/V)}{\partial \rho^2} \right|_{T,c} = \frac{k_B T}{\rho} M_{\rho\rho}(0), \quad (\text{S2.8})$$

and M_{cc} relates to the Gibbs free energy G via the osmotic stability:

$$\left(\frac{\partial^2 G}{\partial c^2}\right)_{T,P,N} = Nk_B T \left[M_{cc}(0) - \frac{M_{\rho c}(0)^2}{M_{\rho\rho}(0)} \right]. \quad (\text{S2.9})$$

To quantify which mechanism drives the instability (GL condensation vs. LL demixing), we compute the instability angle θ :

$$\tan(\theta) = \frac{2M_{\rho c}(0)}{M_{\rho\rho}(0) - M_{cc}(0)}. \quad (\text{S2.10})$$

If $|\theta| \approx 0$, the instability is predominantly LL demixing; if $|\theta| \approx \pi/2$, it is predominantly GL condensation. The conditions where Eq. (S2.8) is zero defines the Spinodal Surface $T_s(\rho, c)$, and equivalently the conditions to make Eq. (S2.9) zero defines the λ -Surface $T_\lambda(\rho, c)$. Intermediate values indicate a coupled instability[15].

S3 Kinetic Atlas: Topological Regimes

This supplement provides the complete three-dimensional (3D) visualizations of the thermodynamic instability surfaces, $T_{\text{Inst}}(\rho, c)$, and the dynamic arrest surfaces, $T_c(\rho, c)$, for the Symmetrical Binary Mixture (SBM). These plots complement the 2D projections presented in the main text and offer a direct view of the topological changes that occur as the cross-species interaction parameter α is varied.

The classification of these topologies follows the rigorous scheme for binary fluids established by van Konynenburg and Scott [19], and adapted specifically for symmetrical mixtures by Schöll-Paschinger et al. [12] and Köfinger et al. [13]. By varying α , we traverse the global phase diagram, identifying five distinct regimes:

- **Type I-A** ($\alpha > 1$): Pure condensation (demixing is thermodynamically impossible) [20].
- **Type I** ($\alpha \approx 0.8$): Kinetic suppression (demixing exists but is buried).
- **Type II** ($\alpha \approx 0.6$): Emergent demixing (arrest intersects the demixing ridge).
- **Type III** ($\alpha \approx 0.3$): Tricritical merger (coalescence of instability lines).
- **Type IV** ($\alpha \approx 0.0$): Pure demixing (condensation vanishes) [12].

For each topological type, we present two viewing angles: a “Front View” showing the general structure in (c, ρ, T) space, and a “Back View” to highlight features obscured by the primary surface curvature.

The instability surface is defined by the condition $\lambda_1(c, \rho, T) = 0$ (where λ_1 is the smallest eigenvalue of the stability matrix), which marks the onset of either gas-liquid (GL) condensation or liquid-liquid (LL) demixing [11, 20]. The dynamic arrest surface is defined by the divergence of the relaxation time within the Self-Consistent Generalized Langevin Equation (SCGLE) theory [10, 21, 22, 23, 24].

S3.1 Type I-A Topology ($\alpha > 1$): Pure Condensation

Figure S1 illustrates the regime where cross-species attraction dominates ($\alpha = 2.0$), classified as Type I-A in the generalized van Konynenburg and Scott scheme [13]. Thermodynamically, the excess strength of the cross-interaction ($\epsilon_{ij} > \epsilon_{ii}$) creates a strong energetic preference for mixing. As demonstrated analytically by Fantoni et al. [20], the condition for a demixing spinodal cannot be met in this regime because the relative adhesiveness is too high; consequently, the liquid-liquid demixing instability is thermodynamically suppressed. The resulting instability surface

$T_{\text{Inst}}(\rho, c)$ manifests as a single, symmetric *convex dome* centered at the equimolar concentration, corresponding exclusively to Gas-Liquid (GL) condensation driven by total density fluctuations.

Kinetically, the dynamic arrest surface (represented by the blue wireframe) intersects this condensation dome, reproducing the topology characteristic of *arrested spinodal decomposition* observed in simple attractive fluids [16]. This intersection implies that deep quenches into the unstable region lead to gelation arrested by local caging and bonding, rather than phase separation. This topology confirms that in the limit of strong cross-attraction, the binary nature of the system is effectively masked. The solidification is driven solely by density fluctuations ($S_{\rho\rho}$) without competition from concentration fluctuations (S_{cc}), reducing the phenomenological behavior to that of an effective single-component fluid.

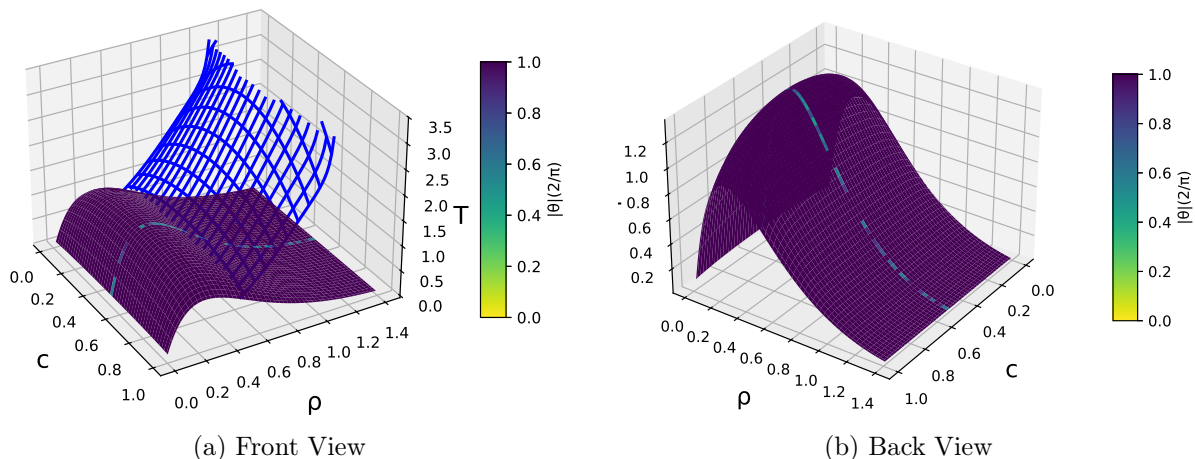


Figure S1: Type I-A Topology ($\alpha = 2.0$): Pure Condensation. The 3D instability surface $T_{\text{Inst}}(\rho, c)$ manifests as a single, symmetric convex dome centered at equimolar concentration. The surface coloration, mapped to the instability angle $|\theta|$, is uniformly dark, indicating that the instability is driven exclusively by total density fluctuations (Gas-Liquid condensation). This topology confirms the analytical prediction [20] that strong cross-attraction ($\alpha > 1$) renders demixing thermodynamically impossible. The dynamic arrest surface T_c (blue mesh) intersects this condensation dome, predicting a direct transition from fluid to a homogeneous attractive glass via arrested spinodal decomposition.

S3.2 Type I ($\alpha \approx 0.8$): Kinetic suppression

As the cross-species interaction strength decreases to $\alpha = 0.8$, the system transitions into the Type I topological regime, following the classification of Schöll-Paschinger et al. [12] and Köfinger et al. [13]. Thermodynamically, the instability landscape remains dominated by a prominent Gas-Liquid (GL) condensation dome. However, unlike the Type I-A regime, a latent Liquid-Liquid (LL) demixing instability now exists. This instability surface is located at low temperatures, buried deep within the high-density region of the phase diagram. The intersection of the demixing line with the condensation binodal defines a Critical End Point (CEP) which, in this regime, lies significantly below the liquid-vapor critical temperature ($T_{\text{CEP}} < T_{\text{cr}}$) [25].

Kinetically, this regime is characterized by the phenomenon of *Kinetic Suppression*. The dynamic arrest surface, $T_c(\rho, c)$ (represented by the blue wireframe in Fig. S2), is positioned strictly above the nascent demixing instability. This topological arrangement has profound physical consequences: for any isochoric quench from the fluid phase, the system inevitably intersects the glass transition line before it can access the thermodynamic demixing instability. Consequently, the slow dynamics effectively “hides” the thermodynamic drive for phase separation. The arrest surface acts as a kinetic shield, trapping the system in a homogeneous *double glass* strictly before

the thermodynamic preference for demixing can manifest.

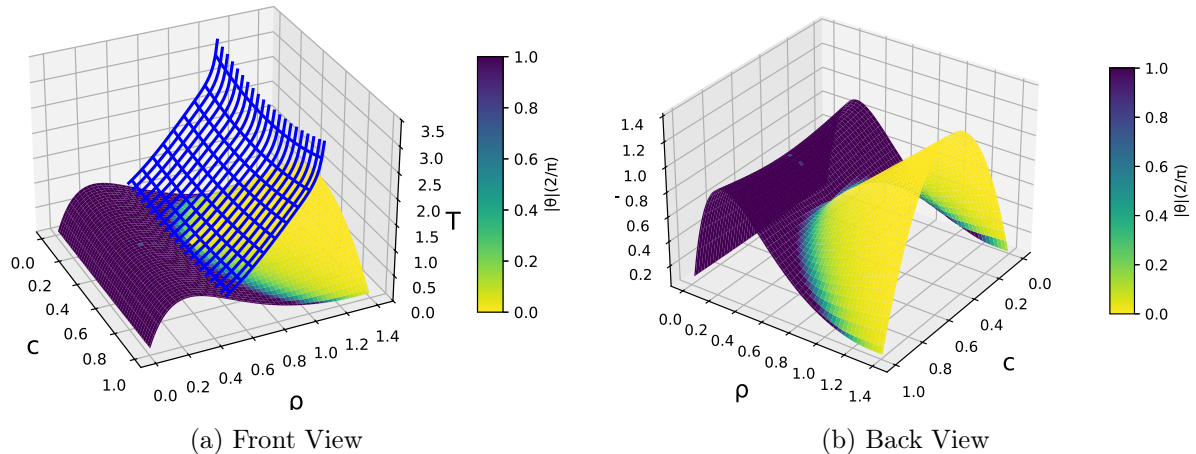


Figure S2: Type I Topology ($\alpha = 0.8$): Kinetic Suppression. The 3D thermodynamic instability surface is dominated by the dark Gas-Liquid (GL) condensation dome. Consistent with the Type I classification [13], a latent Liquid-Liquid (LL) demixing instability (lighter region) exists but is buried deep at low temperatures, with a Critical End Point (CEP) located significantly below the liquid-vapor critical temperature ($T_{CEP} < T_{cr}$). Crucially, the dynamic arrest surface T_c (blue mesh) lies strictly above this latent demixing region. This topology visualizes the phenomenon of *Kinetic Suppression*: the glass transition acts as a kinetic shield, trapping the system in a homogeneous *double glass* state strictly before it can access the thermodynamic driving force for phase separation.

S3.3 Type II ($\alpha \approx 0.6$): Emergent demixing

Figure S3 captures the transition to the Type II topological regime ($\alpha = 0.6$), corresponding to the classification established by Köfinger et al. [13]. In this regime, the thermodynamic landscape undergoes a critical topological shift: as the self-attraction becomes comparable to the cross-attraction, the previously buried liquid-liquid (LL) demixing instability rises significantly in temperature, eventually piercing the gas-liquid (GL) condensation dome. This emergence manifests visually as a distinct “demixing ridge” (lighter color) that disrupts the smooth convex curvature of the condensation surface. The precise intersection of the GL and LL instability surfaces defines a line of Critical End Points (CEP), which shifts toward higher temperatures as α decreases [25].

Kinetically, this regime marks the *breakdown of suppression* and the onset of a *Kinetic Bifurcation* [26, 27, 28, 16, 29]. Unlike the Type I case where the glass transition completely shields the demixing instability, the dynamic arrest surface T_c (blue wireframe) now intersects the emerging demixing ridge at high densities. This topology creates a fork in the system’s kinetic fate determined by the quench density: a quench at low density encounters the condensation dome first, leading to a gel formed by arrested spinodal decomposition; conversely, a quench at high density intersects the exposed demixing ridge first, driving the system toward arrested phase separation. This bifurcation confirms that the emergence of the demixing instability creates a new window for gelation driven by concentration fluctuations (S_{cc}), distinct from the density-driven arrest ($S_{\rho\rho}$) of the monodisperse limit.

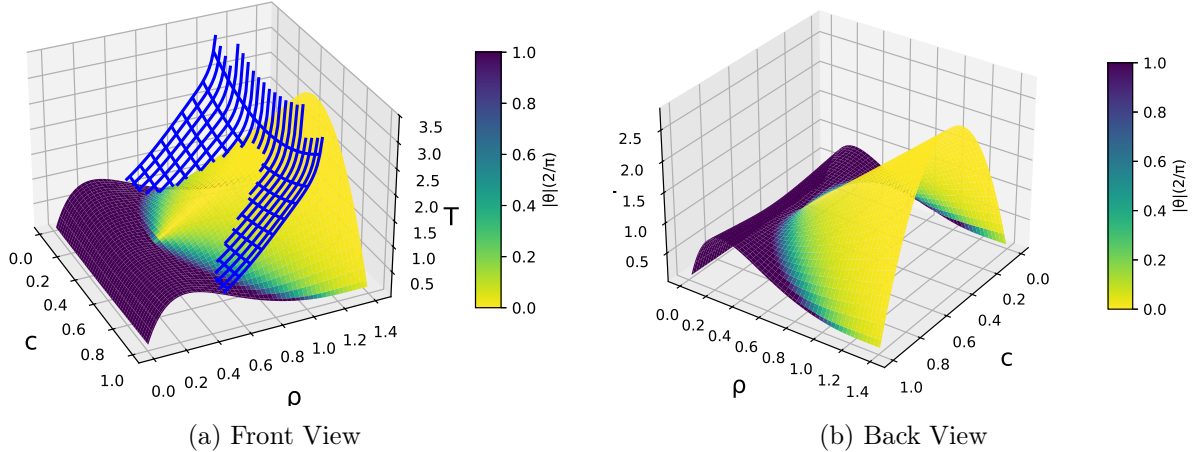


Figure S3: Type II Topology ($\alpha = 0.6$): Emergent Demixing. As the cross-species attraction weakens, the system transitions to the Type II regime [13]. Thermodynamically, the liquid-liquid demixing instability rises in temperature, piercing the gas-liquid condensation dome. This is visualized by the emergence of a light-colored ridge (indicating concentration-driven instability, $|\theta| \approx 0$) disrupting the smooth, dark condensation surface (density-driven, $|\theta| \approx \pi/2$). The intersection of these surfaces marks the Critical End Point (CEP) [25]. Kinetically, the arrest surface T_c (blue mesh) now intersects this exposed demixing ridge. This topology creates a **kinetic bifurcation**: unlike Type I, high-density quenches now access the demixing instability before arrest, opening a pathway for gelation driven by arrested phase separation.

S3.4 Type III ($\alpha \approx 0.3$): Tricritical merger

Figure S4 illustrates the Type III regime ($\alpha = 0.3$), defined by the coalescence of instability mechanisms. As the cross-species interaction strength drops further, the miscibility gap expands significantly, leading to a fundamental topological change described by Schöll-Paschinger et al. [12]: the gas-liquid (GL) and liquid-liquid (LL) instability lines merge at a Tricritical Point (TCP). Unlike the Type II regime where the demixing ridge pierces the condensation dome, here the two surfaces fuse into a continuous sheet [30]. Thermodynamically, this implies that at the TCP, the three coexisting phases (vapor, A-rich liquid, and B-rich liquid) become identical simultaneously. Across this continuous surface, the instability mechanism transitions smoothly from density-driven at the flanks ($|\theta| \approx \pi/2$) to concentration-driven at the center ($|\theta| \approx 0$).

Kinetically, this regime is marked by a significant flattening of the dynamic arrest surface T_c . The characteristic deepness in the arrest temperature—prominent in Types I and II due to strong cross-species bonding—diminishes. This reflects the weakening of the cross-species attraction (ϵ_{ij}); as α decreases, the driving force for gelation shifts from local attractive bonding (caging) toward global phase separation, resulting in a kinetic surface that smoothly bridges the density-driven and concentration-driven arrest boundaries.

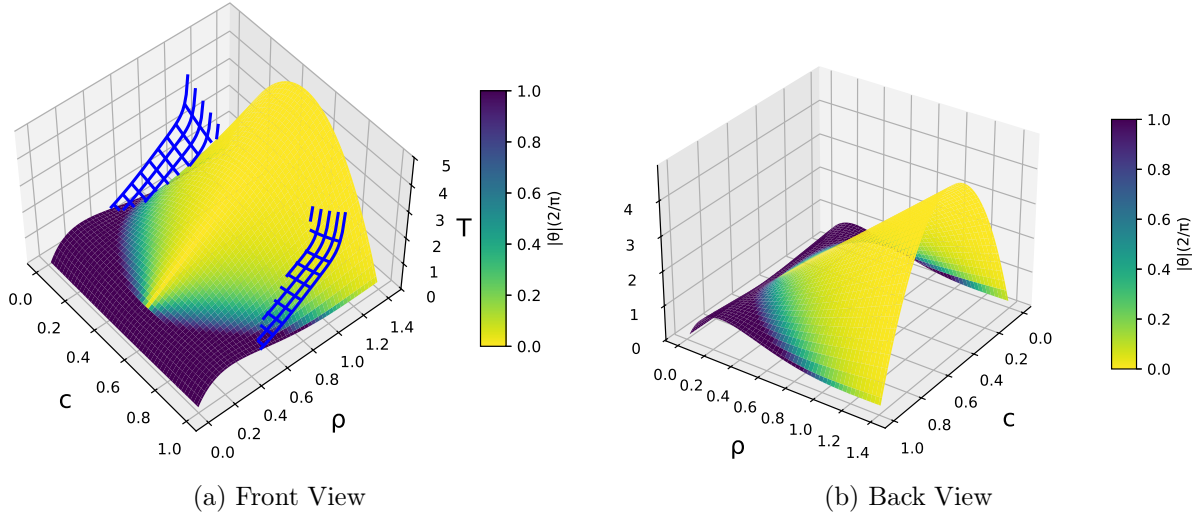


Figure S4: Type III Topology ($\alpha = 0.3$): Tricritical Merger. In this regime, the Gas-Liquid and Liquid-Liquid instability surfaces merge into a single continuous sheet. The point of coalescence defines the *Tricritical Point (TCP)*, where the distinction between condensation and demixing vanishes. Kinetically, the arrest surface (blue mesh) flattens significantly compared to Type I/II. The disappearance of the deep conditions to obtain T_c indicates that the cross-species bonding—which stabilizes the attractive glass in higher α regimes—is no longer sufficient to generate a distinct re-entrant glass transition, leading to a smooth crossover between density-arrested and concentration-arrested states.

S3.5 Type IV ($\alpha \approx 0.0$): Pure demixing

Figure S5 presents the Type IV limit ($\alpha = 0.0$), representing the extreme case of non-interacting species (in terms of attraction), as described by Schöll-Paschinger et al. [12]. Thermodynamically, the absence of cross-species attraction ($\epsilon_{ij} \rightarrow 0$) renders mixing purely entropic and highly unfavorable compared to the energetic gain of self-association. Consequently, the convex Gas-Liquid condensation dome vanishes entirely. It is replaced by vertical instability sheets that extend toward zero density, indicating that the system is unstable to phase separation at nearly all temperatures and densities. In this regime, the instability is driven exclusively by concentration fluctuations (S_{cc}), corresponding to a mechanism of Pure Demixing [20].

Kinetically, this regime exhibits a dramatic Kinetic Decoupling. While thermodynamics predicts demixing instability across a vast region of the phase diagram, the dynamic arrest surface transforms into a *vertical wall* fixed at the Hard-Sphere glass transition density ($\phi_g \approx 0.58$) [8, 31]. Unlike the Type I or II regimes, where strong cross-attraction (ϵ_{ij}) facilitates gelation at low densities via an attractive glass mechanism, the absence of cross-linking in the Type IV limit prevents low-density arrest. The system faces a binary fate: it either phase separates completely via fluid-fluid demixing or, at sufficiently high total packing fractions, jams into a repulsive glass driven solely by excluded volume interactions.

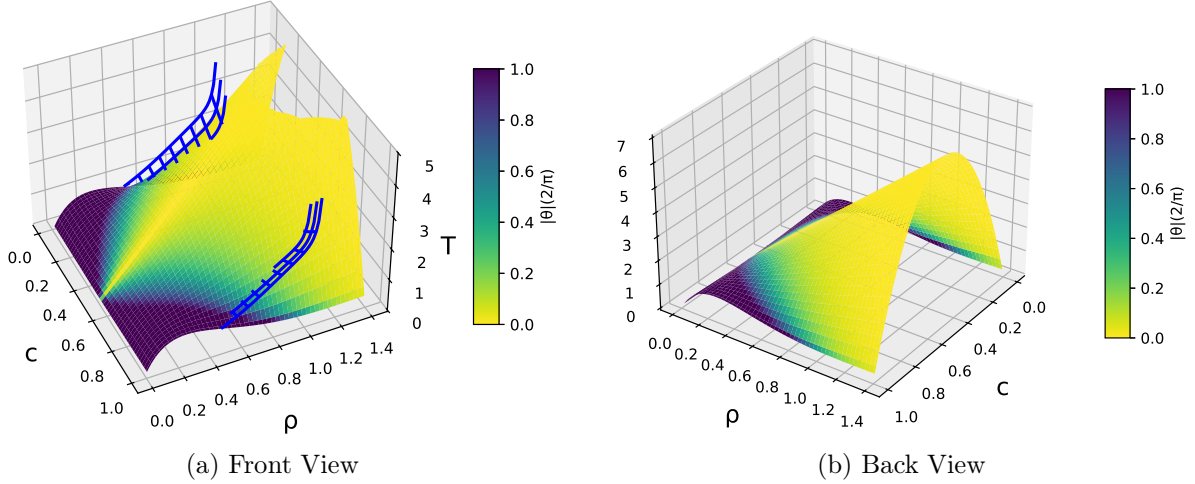


Figure S5: Type IV Topology ($\alpha = 0.0$): Pure Demixing. In the limit of zero cross-species attraction, the thermodynamic landscape is fundamentally altered: the condensation dome vanishes, replaced by vertical sheets indicating a pure demixing instability (S_{cc}) that extends to low densities. Kinetically, the arrest surface (blue mesh) decouples from the temperature-dependent attraction and becomes a vertical wall located at the hard-sphere glass transition density. This topology confirms that without cross-species attraction to form a stabilizing network (attractive glass), the system cannot arrest at low densities and instead undergoes macroscopic phase separation until the high-density repulsive glass limit is reached.

S3.6 Iso-Temperature Contour Maps

Figure S6 presents complementary 2D projections of the instability surface $T_{\text{inst}}(\rho, c)$ onto the concentration-density plane for selected isotherms. These contour maps visualize the evolution of the *miscibility gap* across the topological regimes:

- **Condensation Dominance** ($\alpha \geq 0.9$): For Type I-A ($\alpha = 2.0$) and Type I ($\alpha = 0.9$), the isotherms form closed, concentric loops centered around the critical density. This topology is characteristic of gas-liquid condensation, where the instability is bounded in both density and concentration.
- **Emergence of Demixing** ($\alpha \in [0.7, 0.4]$): As the system traverses the Type II ($\alpha = 0.7, 0.6$) and Type III ($\alpha = 0.4$) regimes, the contours at high densities begin to flatten and widen. This distortion signifies the emergence of the liquid-liquid demixing instability (S_{cc}), which competes with and eventually disrupts the condensation dome [13, 25].
- **Pure Demixing** ($\alpha = 0.0$): In the Type IV limit, the contours transform into vertical lines (parallel to the density axis). This indicates that the instability condition becomes independent of total density and is driven exclusively by concentration fluctuations, consistent with the behavior of non-interacting species where mixing is purely entropic [12].

The solid blue squares mark the specific state points (ρ, c) where the thermodynamic instability surface intersects the dynamic arrest surface T_c . These points define the *kinetic locus* of the system: they represent the highest temperature at which the system encounters thermodynamic instability before arresting into a glass.

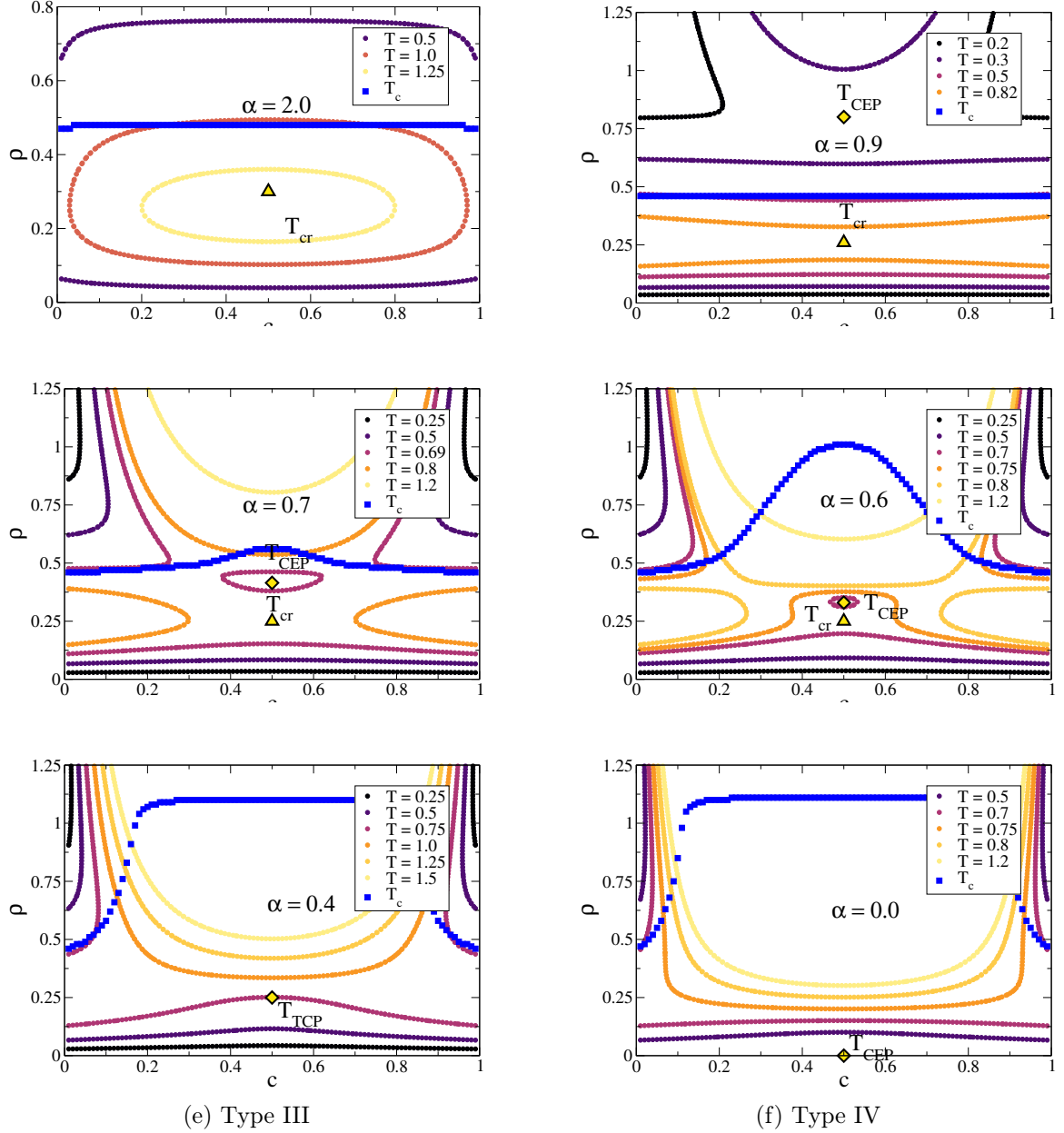


Figure S6: Evolution of the Miscibility Gap. Iso-temperature contours of the instability surface $\lambda_1(c, \rho, T) = 0$ projected onto the (ρ, c) plane for varying interaction strengths α . Lighter lines indicate higher temperatures. (a-b) In the condensation-dominated regimes, contours form closed loops characteristic of simple fluids. (c-d) The emergence of demixing (Type II) distorts the high-density contours. (f) In the Type IV limit, contours become vertical lines, indicating a pure demixing instability driven solely by concentration. Solid blue squares marks the intersection of the instability surface T_{inst} with the dynamic arrest surface T_c , locating the thermodynamic state points where the glass transition intervenes in the phase separation process.

Finally, here is Table 1 summarizing the main relations between the classification topology by Konynenburg and Scott [19, 12, 13], and the kinetic perspective by the SCGLE theory[10, 21].

Table 1: Proposed Kinetic Atlas Classification. This table aligns the interaction parameter α used in this work with the standard thermodynamic topological classifications of van Konynenburg and Scott [19] and Köfinger [13]. The “Physical Name” column establishes the terminology used to describe the specific non-equilibrium phenomena observed in our NESCGLE results.

Energy Ratio ($\alpha = \epsilon_{ij}/\epsilon_{ii}$)	Literature Type	Physical Name (This Work)	Key Topological & Kinetic Feature
$\alpha > 1.0$	Type I-A	Pure Condensation	<i>Demixing is thermodynamically impossible.</i> Cross-attraction dominates; the demixing spinodal solution vanishes [20]. Arrest is driven strictly by density fluctuations ($S_{\rho\rho}$).
$\alpha \approx 0.8$	Type I	Kinetic Suppression	<i>Demixing exists but is buried.</i> The Critical End Point (CEP) lies deep within the spinodal. The glass transition line T_c envelopes the instability, kinetically suppressing phase separation.
$\alpha \approx 0.6$	Type II	Emergent Demixing	<i>Competition regime.</i> The demixing instability (T_λ) rises in temperature. T_c intersects the instability surface near the CEP [25], creating a window for gelation driven by phase separation.
$\alpha \approx 0.3$	Type III	Tricritical Merger	<i>Coalescence.</i> The Gas-Liquid and Liquid-Liquid instability lines merge at a Tricritical Point (TCP). Arrest is driven by a hybrid of density and concentration fluctuations.
$\alpha \approx 0.0$	Type IV	Pure Demixing	<i>Condensation vanishes.</i> In the absence of cross-attraction, the GL dome disappears. Instability is driven exclusively by Liquid-Liquid demixing (S_{cc}), bounded by hard-sphere glass dynamics.

S4 The “Glass-Glass” Transition Line

In this section, we present the results of a systematic evaluation of the asymptotic localization length (defined in eq. (S1.9)), $\gamma^{(a)}$, for a set of independent isochoric thermal quenches. Each quench proceeds from a common initial temperature $T_i = 10.0$ (well within the fluid region) to a variable final temperature T .

Figure S7 displays the dynamic arrest diagrams and the corresponding inverse localization lengths for two distinct interaction regimes: the strong cross-attraction case ($\alpha = 2.0$, condensation-dominated) and the competitive interaction case ($\alpha = 0.5$, demixing rise).

S4.1 Case $\alpha = 0.8$

The arrest diagram in Fig. S7(a) shows the spinodal temperature T_s (solid red line), the λ -line T_λ (solid green line), and the critical arrest temperature T_c (solid blue line).

Figure S7(b) details the behavior of the inverse asymptotic localization length, $1/\gamma^{(a)}$, as a function of the final quench temperature T for three representative isochores. For high-density isochores ($\rho = 0.5$ and 0.75) that do not intersect the spinodal region ($\rho > \rho_b$), the system undergoes a direct transition from an ergodic fluid to a non-ergodic glass. As the temperature

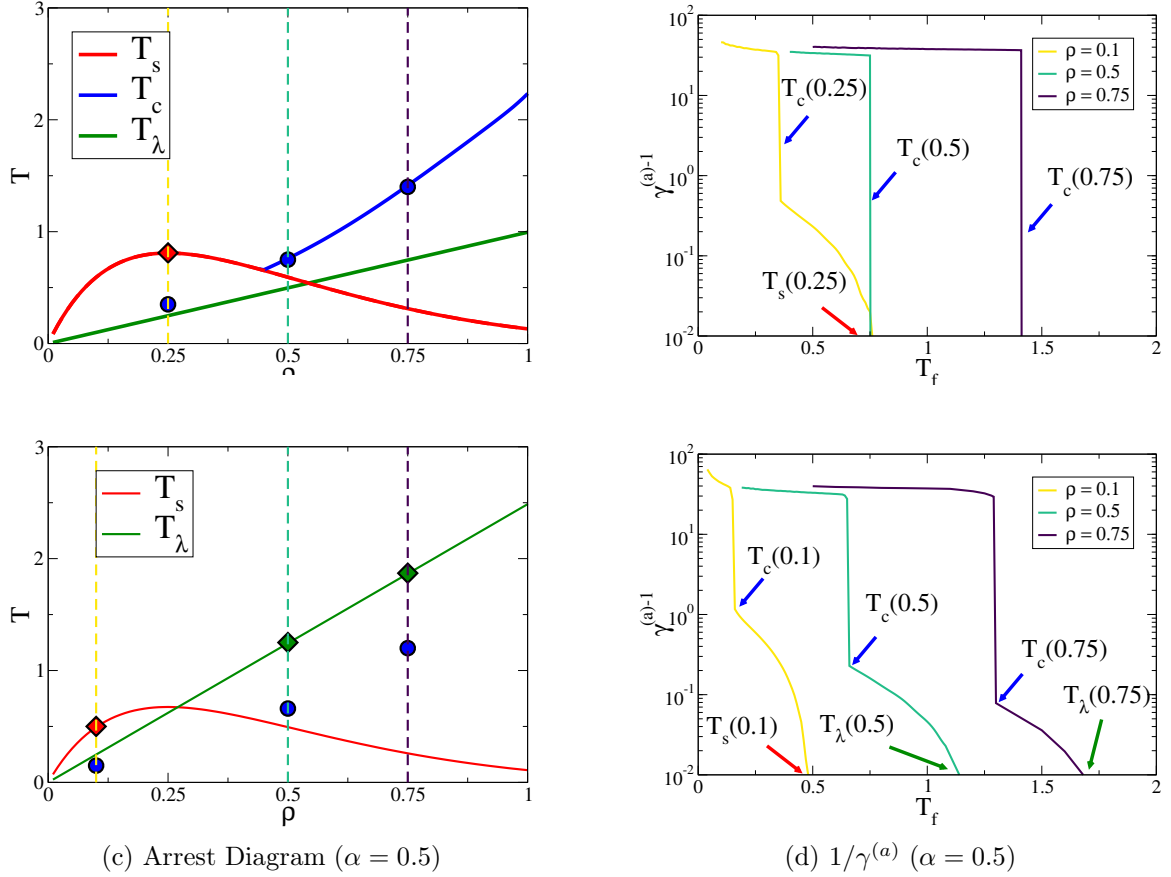


Figure S7: (a) Equilibrium SCGLE arrest diagram for the SBM ($c = 0.5, \alpha = 2.0$). Dashed red line: Spinodal T_s . Solid blue line: Critical arrest temperature T_c . (b) Inverse asymptotic localization length $1/\gamma^{(a)}$ vs. temperature for selected isochores at $\alpha = 2.0$. (c) Arrest diagram for $\alpha = 0.5$. Dashed green line: Demixing λ -line T_λ . (d) Inverse asymptotic localization length $1/\gamma^{(a)}$ vs. temperature for selected isochores at $\alpha = 0.5$.

T decreases, $1/\gamma^{(a)}$ jumps discontinuously from zero to a finite value on the order of 10^2 , corresponding to a localization length of $\sqrt{\gamma^{(a)}} \sim 0.1\sigma$. This discontinuity marks the *ideal glass transition* at T_c , where particle motion changes abruptly from diffusive exploration of the entire volume to localization within a cage approximately 10% of the particle diameter [8].

In contrast, the low-density isochore ($\rho = 0.25$) intersects the spinodal line T_s , resulting in a fundamentally different arrest scenario. As the temperature is lowered towards T_s , the transition from the ergodic fluid is *continuous*, characterized by $1/\gamma^{(a)}$ rising smoothly from zero, which indicates a critical slowing down associated with the thermodynamic instability. However, at a lower temperature $T_c < T_s$, a second, discontinuous jump in $1/\gamma^{(a)}$ is observed. In the intermediate regime $T_c < T < T_s$, the inverse localization length is of the order 10^{-2} (corresponding to $\sqrt{\gamma^{(a)}} \sim 10\sigma$), implying that particles are confined to mesoscopic domains rather than the tight cages of a glass. This signature is characteristic of gel formation or arrested spinodal decomposition [26].

S4.2 Case $\alpha = 0.5$

Figure S7(c) presents the arrest diagram for $\alpha = 0.5$. Here, a second instability line appears: the λ -line (dashed green), indicating the onset of demixing. The dynamic arrest line T_c intersects this λ -line at a critical density $\rho \approx 1.1$.

Figure S7(d) shows the corresponding localization lengths for the isochores $\rho = 0.1, 0.5$, and

0.75. For the intermediate and high densities ($\rho = 0.5$ and 0.75), the isochores intersect the λ -line before reaching the arrest line. Similar to the spinodal crossing observed in the $\alpha = 2.0$ case, we observe a two-step arrest process. First, a continuous transition at T_λ marks the onset of demixing kinetics, where $1/\gamma^{(a)}$ becomes finite but small ($\sim 10^{-1}$). Subsequently, at a lower temperature $T_c < T_\lambda$, a discontinuous jump occurs as the dense, demixed phase undergoes structural arrest. In contrast, the low-density isochore ($\rho = 0.1$) intersects the Gas-Liquid spinodal T_s . The behavior here mirrors the $\alpha = 2.0$ case, characterized by a continuous transition at T_s followed by a discontinuous glass transition at T_c .

By systematically mapping these transitions across all isochores and interaction parameters α , we identify that the lower critical temperature $T_c(\rho)$ (where the discontinuous jump occurs inside the instability region) is the continuation of the liquid-glass transition line $T_c(\rho)$ from the stable fluid region. This line defines a “glass-glass” transition separating two distinct non-ergodic states: the mesoscopically arrested gel/spinodal state (bounded by T_s or T_λ) and the microscopically arrested attractive glass (bounded by T_c).

S5 Structural Overview

In this supplemental, we provide a more detailed characterization than the main text, focused on the representation of fluctuation correlations.

S5.1 Quenches into the Condensation Region

An additional characteristic that can be studied using the asymptotic material time $u^{(a)}$ is the asymptotic structure factor, defined as $\mathbf{S}^{(a)}(k) = \mathbf{S}(k; u^{(a)})$. The elements of this matrix, given by $S_{ij}^{(a)}(k) = \lim_{t \rightarrow \infty} (1/N) \langle \delta\rho_i(k; t) \delta\rho_j(-k; t) \rangle^{ss}$, represent the long-time correlations of the density fluctuations between species i and j .

Following the Chen-Forstmann formalism [11], we adapt their representation to evaluate the asymptotic structure factors in the number-concentration basis. The transformed correlations take the form:

$$S_{\rho\rho}^{(a)}(k) = c_A S_{AA}^{(a)}(k) + c_B S_{BB}^{(a)}(k) + 2\sqrt{c_A c_B} S_{AB}^{(a)}(k), \quad (\text{S5.1})$$

$$S_{cc}^{(a)}(k) = c_B S_{AA}^{(a)}(k) + c_A S_{BB}^{(a)}(k) - 2\sqrt{c_A c_B} S_{AB}^{(a)}(k), \quad (\text{S5.2})$$

$$S_{\rho c}^{(a)}(k) = \sqrt{c_A c_B} \left(S_{AA}^{(a)}(k) - S_{BB}^{(a)}(k) \right) - (c_A - c_B) S_{AB}^{(a)}(k). \quad (\text{S5.3})$$

In Figure S8, we examine the asymptotic structure factor using both the partial species representation ($S_{ii}^{(a)}$) and the number-concentration representation ($S_{\rho\rho}^{(a)}$ and $S_{cc}^{(a)}$) for the cross-interaction parameter $\alpha = 0.5$, equimolar concentration $c = 0.5$, and the isochore $\rho = 0.1$. This density allows us to explore the system’s behavior within the condensation instability (Region III). We present results for four independent quenches to final temperatures $T_f = 0.4, 0.3, 0.2$, and 0.1 .

Figure S8(a) specifically illustrates the effect of a shallow quench to $T_f = 0.4$, slightly below the spinodal temperature ($T_s = 0.48$). The partial structure factors $S_{ii}^{(a)}(k)$ (solid black lines) exhibit a prominent peak at low wave-vectors, $k_{IRO} \simeq 0.5$. This peak, indicative of Intermediate Range Order (IRO) structures, is significantly higher than the main structural peak at $k_{main} \simeq 2\pi$ (i.e., $S_{ii}^{(a)}(k_{IRO}) > S_{ii}^{(a)}(k_{main})$). In the number-concentration representation, the total density-density correlation $S_{\rho\rho}^{(a)}(k)$ (dashed blue lines) follows the same trend, displaying a pronounced low- k peak. The concentration-concentration correlation $S_{cc}^{(a)}(k)$ (dashed red curves) also exhibits this feature, but with a much lower intensity; notably, $S_{\rho\rho}^{(a)}(k_{IRO}) \gg S_{cc}^{(a)}(k_{IRO})$. Finally, for the equimolar concentration ($c = 0.5$), the cross-correlation term vanishes identically ($S_{\rho c}^{(a)}(k) = 0$ for all k) due to symmetry [Eq. (S5.3)].

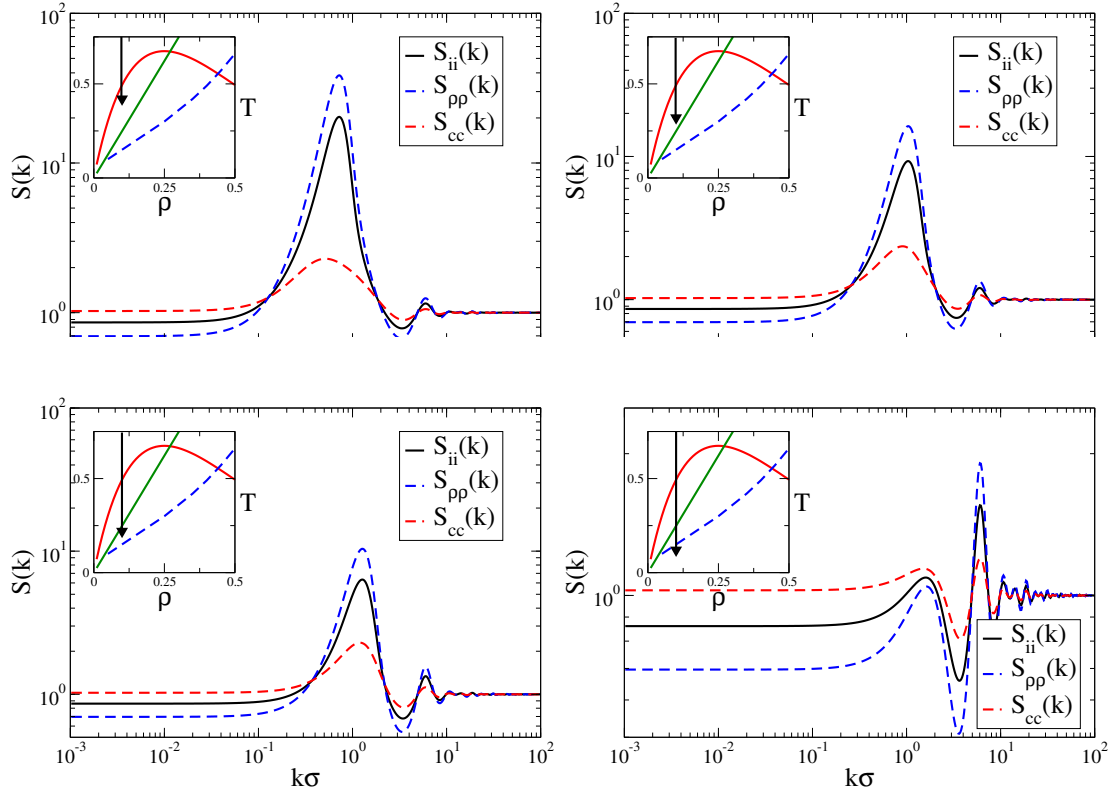


Figure S8: Asymptotic structure factors for the isochore $\rho = 0.1$ in two representations: $S_{ii}(k) \equiv (1/N) \langle \delta\rho_i(k)\delta\rho_i(-k) \rangle$ (solid black lines); $S_{pp}(k) \equiv (1/N) \langle \delta\rho(k)\delta\rho(-k) \rangle$ (dashed blue lines), and $S_{cc}(k) \equiv (1/N) \langle \delta c(k)\delta c(-k) \rangle$ (dashed red lines). The final temperature of each independent quench is (a) $T = 0.4$, (b) 0.3 , (c) 0.2 , and (d) 0.1 . (Inset) Non-Equilibrium Arrest diagram from Figure 1(b) if the main text, with the final temperature indicated by a solid green triangle.

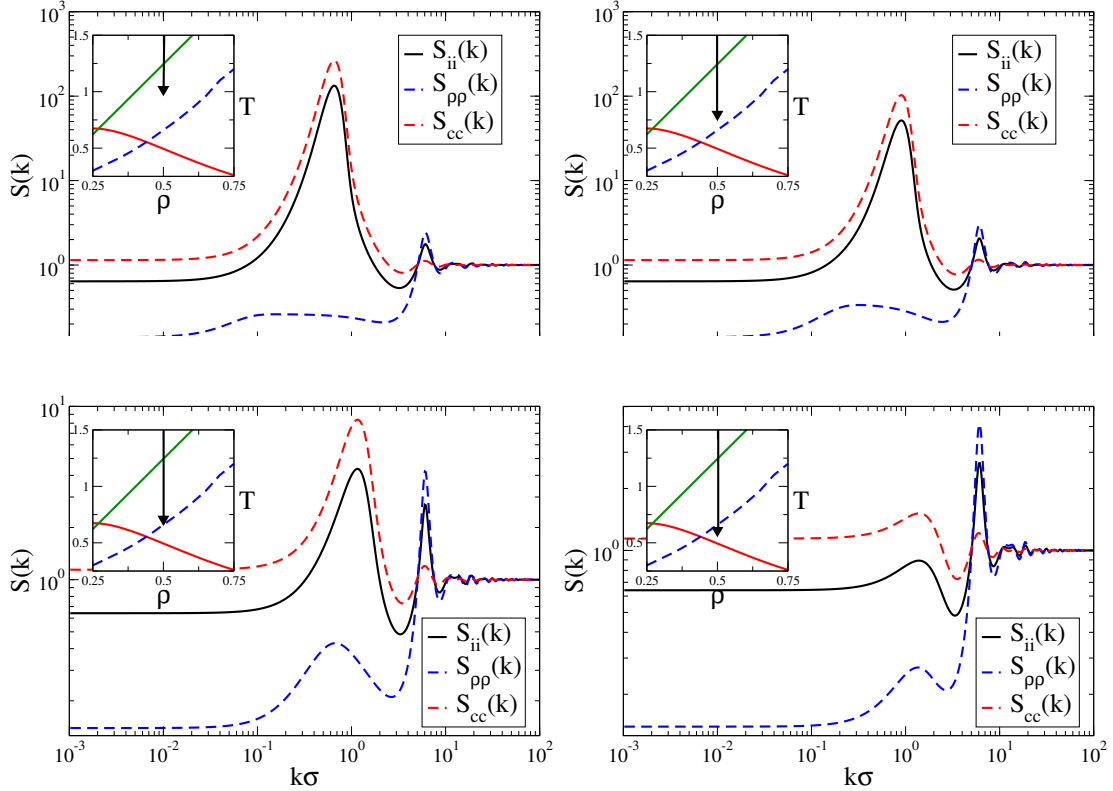


Figure S9: Asymptotic structure factors for the isochore $\rho = 0.5$ in two representations: The (ρ_1, ρ_2) -representation $S_{ii}(k)$ (solid black lines); and the (c, ρ) -representation $S_{\rho\rho}(k)$ (dashed blue lines) and $S_{cc}(k)$ (dashed red lines). The final temperature of each independent quench is (a) $T = 1.0$, (b) 0.8 , (c) 0.64 , and (d) 0.6 . (Inset) Non-Equilibrium Arrest diagram from Figure 1(b) if the main text, with the final temperature indicated by a solid green triangle.

As we lower the temperature, the magnitude of $S_{\rho\rho}^{(a)}(k_{IRO})$ decreases as the final temperature approaches the λ -line at $T_\lambda = 0.29$. Figures S8(b) and (c) illustrate the system's behavior as it crosses this threshold (for $T_f = 0.3$ and 0.2 , respectively); remarkably, we observe no qualitative influence of the transition temperature on the structural evolution. The most notable characteristic of this cooling process is the significant suppression of the IRO peak height, which drops by nearly an order of magnitude. In contrast, crossing the dynamic arrest line ($T_c = 0.12$) has a profound impact on the asymptotic structure. As shown in Fig. S8(d) for $T_f = 0.1 < T_c$, the IRO peak is suppressed to such an extent that the main structural peak becomes the dominant feature.

Throughout this regime, the number-number structure factor, $S_{\rho\rho}^{(a)}$, effectively captures the dominant behavior observed in the partial structure factors, $S_{ii}^{(a)}$. This consistency reflects the physical nature of the spinodal line $T_s(\rho)$, which arises specifically from instabilities in density correlations.

S5.2 Quenches into the Demixing Region

Next, we explore the behavior within the demixing regime (Region IV). In Figure S9, we plot the asymptotic structure factor for the isochore $\rho = 0.5$. First, Figure S9(a) shows the result for a final temperature of $T_f = 1.0$, which lies below the λ -line ($T_\lambda = 1.45$). We then progressively decrease the temperature to $T_f = 0.8$ and 0.64 (Figs. S9(b) and (c), respectively), remaining above the dynamic arrest temperature $T_c = 0.62$. Finally, in Figure S9(d), we present the case where the temperature is lowered to $T_f = 0.6$, crossing into the arrested regime ($T_f < T_c$).

Focusing first on the partial structure factors $S_{ii}^{(a)}$ (solid black lines), we observe only the formation of IRO structures associated with the low- k peak, which is notably suppressed below the transition line $T_c(\rho)$. However, the number-concentration representation provides a much richer perspective, revealing a complete inversion of the roles of the two fluctuation modes compared to the previous case. Here, in the demixing Region IV, the concentration-concentration structure factor $S_{cc}^{(a)}$ (dashed red line) dominates the behavior, reflecting the strong concentration fluctuations characteristic of demixing. Crucially, below the arrest temperature T_c , the main structural peak is almost entirely accounted for by the density correlations $S_{\rho\rho}^{(a)}$ (dashed blue line). This behavior effectively decouples the nature of the two peaks: the low- k IRO peak is driven by concentration fluctuations (demixing), while the high- k main peak is driven by density fluctuations (local packing/arrest).

Note that the partial structure factors in Fig. S8 (condensation) and Fig. S9 (demixing) exhibit nearly identical low- k features, confirming the structural blindness hypothesis. The scenarios depicted in Figures S8 (predominantly condensation) and S9 (predominantly demixing) reveal the behavior of the static structure factor within the instability regions III and IV. Both regimes share common features: the formation of an IRO peak at low k -values, and its sudden suppression when the final temperature enters the Double Glass region (Region II). Crucially, the partial structure factor representation, $S_{ii}^{(a)}$, is incapable of differentiating the nature of the increased correlations in these two regimes. In contrast, the number-concentration representation provides a clear distinction. In the condensation region, the IRO peak is fully explained by the total density fluctuations ($S_{\rho\rho}^{(a)}$), whereas in the demixing region, the concentration fluctuations ($S_{cc}^{(a)}$) are sufficient to account for the IRO peak.

References

- [1] Pedro Ramírez-González and Magdaleno Medina-Noyola. General nonequilibrium theory of colloid dynamics. *Phys. Rev. E*, 82:061503, Dec 2010.
- [2] Ricardo Peredo-Ortiz, Luis F. Elizondo-Aguilera, Pedro Ramírez-González, Edilio Lázaro-Lázaro, Patricia Mendoza-Méndez, and Magdaleno Medina-Noyola. Non-equilibrium on-sager-machlup theory. *Molecular Physics*, 0(0):e2297991, 2023.
- [3] R. Peredo-Ortiz, E. Lázaro-Lázaro, O. Joaquín-Jaime, M. Medina-Noyola, and L.F. Elizondo-Aguilera. The nonequilibrium self-consistent generalized langevin equation theory of glasses and gels. *Annual Review of Chemical and Biomolecular Engineering*, 2026.
- [4] O. Joaquín-Jaime, R. Peredo-Ortiz, M. Medina-Noyola, and L. F. Elizondo-Aguilera. From equilibrium to nonequilibrium statistical mechanics of liquids. *Phys. Rev. E*, 112:054113, Nov 2025.
- [5] J. P. Hansen and I. R. McDonald. *Theory of Simple Liquids*. Academic Press Inc., 1976.
- [6] D. A. McQuarrie. *Statistical Mechanics*. Harper & Row, 1973.
- [7] P. Mendoza-Méndez, R. Peredo-Ortiz, E. Lázaro-Lázaro, M. Chávez-Paez, H. Ruiz-Estrada, F. Pacheco-Vázquez, M. Medina-Noyola, and L. F. Elizondo-Aguilera. Structural relaxation, dynamical arrest, and aging in soft-sphere liquids. *The Journal of Chemical Physics*, 157(24):244504, 12 2022.
- [8] Luis Enrique Sánchez-Díaz, Pedro Ramírez-González, and Magdaleno Medina-Noyola. Equilibration and aging of dense soft-sphere glass-forming liquids. *Phys. Rev. E*, 87:052306, May 2013.

- [9] Ricardo Peredo-Ortiz, Magdaleno Medina-Noyola, Thomas Voigtmann, and Luis F. Elizondo-Aguilera. “inner clocks” of glass-forming liquids. *The Journal of Chemical Physics*, 156(24):244506, 06 2022.
- [10] R. Juárez-Maldonado and M. Medina-Noyola. Alternative view of dynamic arrest in colloid-polymer mixtures. *Phys. Rev. Lett.*, 101:267801, Dec 2008.
- [11] X. S. Chen and F. Forstmann. The demixing and gas-liquid instability of a binary yukawa fluid. *The Journal of Chemical Physics*, 97(5):3696–3703, 09 1992.
- [12] Elisabeth Schöll-Paschinger and Gerhard Kahl. Type-iv phase behavior in fluids with an internal degree of freedom. *The Journal of Chemical Physics*, 123(13):134508, 10 2005.
- [13] Jürgen Köfinger, Nigel B. Wilding, and Gerhard Kahl. Phase behavior of a symmetrical binary fluid mixture. *The Journal of Chemical Physics*, 125(23):234503, 12 2006.
- [14] James L. Harden, Hongyu Guo, Martine Bertrand, Tyler N. Shendruk, Subramanian Ramakrishnan, and Robert L. Leheny. Enhanced gel formation in binary mixtures of nanocolloids with short-range attraction. *The Journal of Chemical Physics*, 148(4):044902, 01 2018.
- [15] Francesco Varrato, Lorenzo Di Michele, Maxim Belushkin, Nicolas Dorsaz, Simon H. Nathan, Erika Eiser, and Giuseppe Foffi. Arrested demixing opens route to bigels. *Proceedings of the National Academy of Sciences*, 109(47):19155–19160, 2012.
- [16] Jesús Benigno Zepeda-López and Magdaleno Medina-Noyola. Waiting-time dependent non-equilibrium phase diagram of simple glass- and gel-forming liquids. *The Journal of Chemical Physics*, 154(17):174901, 05 2021.
- [17] R.V. Sharma and K.C. Sharma. The structure factor and the transport properties of dense fluids having molecules with square well potential, a possible generalization. *Physica A: Statistical Mechanics and its Applications*, 89(1):213–218, 1977.
- [18] R. J. Baxter. Ornstein–zernike relation and percus–yevick approximation for fluid mixtures. *The Journal of Chemical Physics*, 52(9):4559–4562, 05 1970.
- [19] P. H. van Konynenburg and R. L. Scott. Critical lines and phase equilibria in binary van der waals mixtures. *Philosophical Transactions of the Royal Society of London, Series A: Mathematical and Physical Sciences*, 298(1442):495–540, 12 1980.
- [20] Riccardo Fantoni, Domenico Gazzillo, and Achille Giacometti. Thermodynamic instabilities of a binary mixture of sticky hard spheres. *Phys. Rev. E*, 72:011503, Jul 2005.
- [21] R. Juárez-Maldonado and M. Medina-Noyola. Theory of dynamic arrest in colloidal mixtures. *Phys. Rev. E*, 77:051503, May 2008.
- [22] E. Lázaro-Lázaro, J. A. Moreno-Razo, and M. Medina-Noyola. Anomalous dynamic arrest of non-interacting spheres (“polymer”) diluted in a hard-sphere (“colloid”) liquid. *The Journal of Chemical Physics*, 148(10):104505, 03 2018.
- [23] Nohely Benitez-Camacho, José Manuel Olais-Govea, Leticia López-Flores, and Honorina Ruiz-Estrada. Arrested spinodal decomposition of the screened symmetric restricted primitive model. *The Journal of Chemical Physics*, 159(4):044906, 07 2023.
- [24] Juan C. Avilés-Sánchez, Ernesto C. Cortés-Morales, Mariana E. Farías-Anguiano, Jonathan K. Whitmer, and Pedro E. Ramírez-González. Linking dynamics and structure in highly asymmetric ionic liquids. *Physics of Fluids*, 37(1):017173, 01 2025.

- [25] Enrique Diaz-Herrera, Guillermo Ramirez-Santiago, and Jose A. Moreno-Razo. Phase and interfacial behavior of partially miscible symmetric lennard-jones binary mixtures. *The Journal of Chemical Physics*, 123(18):184507, 11 2005.
- [26] José Manuel Olais-Govea, Leticia López-Flores, and Magdaleno Medina-Noyola. Non-equilibrium theory of arrested spinodal decomposition. *The Journal of Chemical Physics*, 143(17):174505, 11 2015.
- [27] José Manuel Olais-Govea, Leticia López-Flores, Martín Chávez-Páez, and Magdaleno Medina-Noyola. Nonequilibrium kinetics of the transformation of liquids into physical gels. *Phys. Rev. E*, 98:040601, Oct 2018.
- [28] José Manuel Olais-Govea, Leticia López-Flores, Jesús Benigno Zepeda-López, and Magdaleno Medina-Noyola. Interference between the glass, gel, and gas-liquid transitions. *Scientific Reports*, 9(1):16445, Nov 2019.
- [29] Ana Gabriela Carretas-Talamante, Jesús Benigno Zepeda-López, Edilio Lázaro-Lázaro, Luis Fernando Elizondo-Aguilera, and Magdaleno Medina-Noyola. Non-equilibrium view of the amorphous solidification of liquids with competing interactions. *The Journal of Chemical Physics*, 158(6):064506, 02 2023.
- [30] Enrique Díaz-Herrera, J. Antonio Moreno-Razo, and Guillermo Ramírez-Santiago. Wetting phenomenon in the liquid-vapor phase coexistence of a partially miscible lennard-jones binary mixture. *Phys. Rev. E*, 70:051601, Nov 2004.
- [31] P. N. Pusey and W. van Megen. Phase behaviour of concentrated suspensions of nearly hard colloidal spheres. *Nature*, 320(6060):340–342, Mar 1986.